A generalized semi-analytic model for magnetar-driven supernovae

Conor M. B. Omand [1]* and Nikhil Sarin[2,3]

[1]*The Oskar Klein Centre, Department of Astronomy, Stockholm University, AlbaNova, SE-106 91 Stockholm, Sweden*
[2]*Nordita, Stockholm University and KTH Royal Institute of Technology Hannes Alfvéns väg 12, SE-106 91 Stockholm, Sweden*
[3]*The Oskar Klein Centre, Department of Physics, Stockholm University, AlbaNova, SE-106 91 Stockholm, Sweden*

ABSTRACT

Several types of energetic supernovae, such as superluminous supernovae (SLSNe) and broad-line Ic supernovae (Ic-BL SNe), could be powered by the spin-down of a rapidly rotating magnetar. Currently, most models used to infer the parameters for potential magnetar-driven supernovae make several unsuitable assumptions that likely bias the estimated parameters. In this work, we present a new model for magnetar-driven supernovae that relaxes several of these assumptions and an inference workflow that enables accurate estimation of parameters from light curves of magnetar-driven supernovae. In particular, in this model, we include the dynamical evolution of the ejecta, coupling it to the energy injected by the magnetar itself while also allowing for non-dipole spin down. We show that the model can reproduce SLSN and Ic-BL SN light curves consistent with the parameter space from computationally expensive numerical simulations. We also show the results of parameter inference on four well-known example supernovae, demonstrating the model's effectiveness at capturing the considerable diversity in magnetar-driven supernova light curves. The model fits each light curve well and recovers parameters broadly consistent with previous works. This model will allow us to explore the full diversity of magnetar-driven supernovae under one theoretical framework, more accurately characterize these supernovae from only photometric data, and make more accurate predictions of future multiwavelength emission to test the magnetar-driven scenario better.

Key words: stars: magnetars – supernovae: general – supernovae: individual: SN 2015bn – supernovae: individual: SN 2007ru – supernovae: individual: ZTF20acigmel – supernovae: individual: iPTF14gqr.

1 INTRODUCTION

Recent wide-field high-cadence surveys, such as the Zwicky Transient Facility (ZTF; Bellm et al. 2019) and the Asteroid Terrestrial-impact Last Alert System (ATLAS; Tonry 2011; Tonry et al. 2018), can discover more than 1000 supernovae per year (Cappellaro 2022), and next-generation facilities such as Rubin Observatory (Ivezić et al. 2019) will be able to discover more than 1000 supernovae per night (LSST Science Collaboration 2009; Stritzinger & Moriya 2018). Core-collapse supernovae (CCSNe), caused by the deaths of massive stars, tend to have explosion energies of $\sim 10^{51}$ erg and radiated energies $\sim 10^{49}$ erg, which can be well explained by models (Arnett 1980, 1982). However, several classes of CCSNe have energies higher than these standard models. Superluminous supernovae (SLSNe) radiate $\sim$ 10–100 times more energy than a standard CCSN (Gal-Yam 2012; Nicholl 2021) and broad-line Type Ic supernovae (SNe Ic-BL) have inferred kinetic energies $\sim$ 10 times higher than a typical CCSN (e.g. Modjaz, Gutiérrez & Arcavi 2019; Taddia et al. 2019). These energetic supernovae have both been associated with long- or ultra-long gamma-ray bursts (GRBs) (Gendre et al. 2013; Nakauchi et al. 2013; Levan et al. 2014; Cano et al. 2017), and SLSNe and SNe Ic-BL also have similar host

galaxies (Lunnan et al. 2014; Chen et al. 2015; Leloudas et al. 2015a; Angus et al. 2016; Chen et al. 2017; Schulze et al. 2018; Ørum et al. 2020), and have similar spectral features at both early (Pastorello et al. 2010; Inserra et al. 2013; Nicholl et al. 2013; Liu, Modjaz & Bianco 2017; Blanchard et al. 2019) and late (Milisavljevic et al. 2013; Jerkstrand et al. 2017; Nicholl, Guillochon & Berger 2017b) times. Other types of unusually energetic supernovae, such as fast blue optical transients (FBOTs) and bright ultra-stripped supernovae (USSNe), have been suggested to have similar power sources as SLSNe and SNe Ic-BL (Liu et al. 2022; Sawada, Kashiyama & Suwa 2022).

Several different models can be used to explain the high energies of one or both of SLSNe or SNe Ic-BL. Stars with masses $M_* \gtrsim 130 \, M_\odot$ can explode as pair instability supernovae (PISNe) (Barkat, Rakavy & Sack 1967; Heger & Woosley 2002; Gal-Yam et al. 2009), which can generate tens of solar masses of ^{56}Ni and present as an extremely long-lived, luminous supernovae. Slightly less massive stars, with $130 \, M_\odot \gtrsim M_* \gtrsim 100 \, M_\odot$, can eject shells of material through the pair-instability without being completely destabilized, and collisions between the ejected shells can be as luminous as an SLSN (Heger et al. 2003; Woosley, Blinnikov & Heger 2007; Chatzopoulos & Wheeler 2012; Yoshida et al. 2016; Woosley 2017) – these are known as pulsational pair-instability supernovae (PPISNe). The collision of supernova ejecta and circumstellar material surrounding the progenitor, ejected through either a steady wind, eruptive mass-

*E-mail: conor.omand@astro.su.se

loss, or binary interaction (Smith 2014), can convert much of the supernova kinetic energy into radiation, leading to a highly luminous supernova (Chatzopoulos & Wheeler 2012; Chatzopoulos et al. 2013; Villar et al. 2017; Jiang, Jiang & Ashley Villar 2020). Finally, the compact remnant can inject some energy into the ejecta; this energy may come from fallback accretion onto a central black hole or neutron star (Dexter & Kasen 2013; Moriya, Nicholl & Guillochon 2018), a collapsar or jet (MacFadyen & Woosley 1999), or the spin-down energy of a rapidly rotating magnetar (Kasen & Bildsten 2010; Woosley 2010).

In the magnetar model, the spin-down energy is emitted as a highly magnetized particle wind, which expands relativistically until it collides with the inner edge of the supernova ejecta, create forward and reverse shocks. The expanding wind becomes shocked by the reverse shock, accelerating the particles up to ultrarelativistic energies, which then emit via synchrotron radiation and inverse Compton scattering (Gaensler & Slane 2006); this shocked wind is known as a pulsar wind nebula (PWN). The PWN applies a pressure to the supernova ejecta, causing it to accelerate, and the radiation from the nebula is thermalized in the ejecta, causing the ejecta temperature and supernova luminosity to both increase (Kasen & Bildsten 2010). The PWN-ejecta interaction can also cause Rayleigh-Taylor instabilities, which can shred the inner ejecta and cause non-spherical structure to emerge in the ejecta (Suzuki & Maeda 2017, 2021).

The magnetar model predicts many multiwavelength signals that could be used to identify and characterize the newborn neutron star. Once the ejecta becomes optically thin, the non-thermal emission from the PWN can be detected directly, either at high energy in hard X-rays or gamma rays (Kotera, Phinney & Olinto 2013; Murase et al. 2015; Kashiyama et al. 2016), or at low energy in radio (Omand, Kashiyama & Murase 2018; Eftekhari et al. 2021; Murase et al. 2021); two energetic SNe have radio detections at late times that are consistent with PWN emission, PTF10hgi (Eftekhari et al. 2019; Law et al. 2019; Mondal et al. 2020; Hatsukade et al. 2021) and SN2012au (Stroh et al. 2021). Dust formed in the supernova can absorb PWN emission and re-emit that energy in infrared (Omand, Kashiyama & Murase 2019), causing bright continuum emission recently seen in four SLSNe (Chen et al. 2021; Sun, Xiao & Li 2022). High-energy photons and Rayleigh-Taylor induced mixing can change the chemical and ionization structure of the ejecta, leading to unique signatures in the supernova nebular spectrum (Chevalier & Fransson 1992; Omand & Jerkstrand 2023). Aspherical ejecta caused by either hydro instabilities or an aspherical PWN can produce an optical polarization signal (Tanaka et al. 2017), which has been detected in some energetic SNe (Inserra et al. 2016; Saito et al. 2020; Pursiainen et al. 2022; Poidevin et al. 2023; Pursiainen et al. 2023), but not others (Leloudas et al. 2015b; Lee 2019, 2020; Poidevin et al. 2022, 2023; Pursiainen et al. 2023).

Accurate parameter estimation from the light curve around optical peak is essential for a number of reasons. First, new surveys such as the LSST will detect SLSNe out to high redshift, where they cannot all be classified with spectroscopy. Therefore, these supernovae will have to be characterized from their light-curve data alone. Also, predicting late-time multiwavelength signals requires accurate parameter estimation, as different parameters that produce similar optical light curves can produce vastly different multiwavelength signals (e.g. Omand, Kashiyama & Murase 2018, 2019). In most widely used parameter inference codes (e.g. Nicholl, Guillochon & Berger 2017b), the model used for inference of magnetar-driven SNe makes several assumptions to reduce computational complexity, which are unjustified outside a small region of the parameter space.

In particular, they assume a constant ejecta velocity, which is independent of the magnetar luminosity, although numerical simulations show that ejecta acceleration due to PWN pressure plays a vital role in the dynamics of the ejecta (Chen, Woosley & Sukhbold 2016; Suzuki & Maeda 2017, 2019; Chen, Woosley & Whalen 2020; Suzuki & Maeda 2021). They also assume the magnetar spin down through pure vacuum dipole emission, even though studies of Galactic pulsars (Lyne et al. 2015; Parthasarathy et al. 2020) and putative magnetars born in GRBs (Lasky et al. 2017; Sarin, Lasky & Ashton 2020a, b) show that most neutron stars are inconsistent with a pure vacuum dipole.

In this work, we present a model where these assumptions are relaxed, which can fully explore the diversity of magnetar-driven supernovae and unite phenomenologically different supernovae, such as SNe Ic-BL and SLSNe, under one theoretical framework. In Section 2, we introduce our model for magnetar-driven supernovae. In Section 3, we show the diversity of supernovae and supernova observables resulting from differences in initial parameters. In Section 4, we perform Bayesian inference on a few varying supernovae to show how our model can consistently reproduce and explain them. Finally, in Section 5, we discuss the model's implications and conclude. Throughout the paper, we use the notation $Q_x = Q/10^x$ in cgs units unless otherwise noted.

2 MODEL

The physics of our model is based on previous magnetar-driven kilonovae models (e.g. Yu, Zhang & Gao 2013; Metzger 2019; Sarin et al. 2022), but modified to describe supernovae. We present here a non-relativistic model description, although the model implementation is fully relativistic. For the fully relativistic description of the kinematics [equations (5), (6), (14), (16), (17), (18), and (19)], see Sarin et al. (2022). We note that relativistic corrections are largely unimportant for supernovae apart from transients with exceptionally low ejecta masses and powerful magnetar engines.

2.1 Model physics

The central magnetar spins down by releasing its rotational energy

$$E_{\rm rot} = \frac{1}{2}I\Omega^2, \tag{1}$$

where I is the moment of inertia of the magnetar and Ω is the rotational angular frequency of the magnetar. The time derivative of this relation gives the spin down luminosity,

$$L_{\rm SD} = I\Omega\dot{\Omega}, \tag{2}$$

which, given $\dot{\Omega} \propto -\Omega^n$ for braking index n, can be modelled generally as (Lasky et al. 2017)

$$L_{\rm SD}(t) = L_0 \left(1 + \frac{t}{t_{\rm SD}}\right)^{\frac{1+n}{1-n}}, \tag{3}$$

where L_0 is the initial magnetar spin-down luminosity and $t_{\rm SD}$ is the magnetar spin-down time. The vacuum dipole spin-down mechanism (Goldreich & Julian 1969; Ostriker & Gunn 1969) has a corresponding braking index of $n = 3$, which gives a late-time spin-down down luminosity of $L \propto t^{-2}$ (Zhang & Mészáros 2001), while gravitational wave spin down via magnetic deformation (Cutler & Jones 2000) has a corresponding braking index of $n = 5$, and has a late-time spin-down luminosity of $L \propto t^{-3/2}$. There are also several other mechanisms for spin down, including particle winds (Harding, Contopoulos & Kazanas 1999; Xu & Qiao 2001; Wu, Xu & Gil 2003;

Contopoulos & Spitkovsky 2006), multipolar radiation (Pétri 2015), and r-mode oscillations (Ho & Lai 2000), among others (Blandford & Romani 1988; Lin & Zhang 2004; Ruderman 2005; Chen & Li 2006; Contopoulos 2007; Yue, Xu & Zhu 2007), and several mechanisms can spin-down the magnetar simultaneously. We note that in general, n is also expected to be variable during the early life of the magnetar (Lander & Jones 2018, 2020), but we keep it constant for simplicity. Integrating equation (3) gives the total rotational energy as a function of braking index:

$$E_{\rm rot} = \frac{n-1}{2} L_0 t_{\rm SD}. \qquad (4)$$

This recovers $E_{\rm rot} = L_0 t_{\rm SD}$ for vacuum dipole spin-down.

The rotational energy from the magnetar is converted into a pulsar wind. This highly magnetized, ultrarelativistic wind collides with and pushes a shock into the supernova ejecta, increasing its kinetic and internal energy. The internal energy is also increased by the absorption of PWN photons by the ejecta. The total energy of the system is the combination of the kinetic and internal energy

$$E_{\rm ej} = \frac{1}{2} M_{\rm ej} v_{\rm ej}^2 + E_{\rm int}, \qquad (5)$$

where $M_{\rm ej}$ is the ejecta mass. The evolution of this system is governed by the energy sources, radioactive heating, and magnetar spin-down luminosity, and energy losses from radiated luminosity and adiabatic cooling from expansion. The evolution of the internal energy of the ejecta is written as (Kasen, Metzger & Bildsten 2016)

$$\frac{{\rm d}E_{\rm int}}{{\rm d}t} = \xi L_{\rm SD} + L_{\rm ra} - L_{\rm bol} - \mathcal{P}\frac{{\rm d}V}{{\rm d}t}, \qquad (6)$$

where $L_{\rm ra}$ and $L_{\rm bol}$ are the radioactive power and emitted bolometric luminosity, respectively, ξ is the fraction of spin-down luminosity injected into the ejecta, and $\mathcal{P}$ and V are the pressure and volume of the ejecta.

Here, we adopt the Wang et al. (2015) prescription for gamma-ray leakage used in other models (e.g. Nicholl, Guillochon & Berger 2017b; Sarin et al. 2022) with

$$\xi = 1 - e^{-At^{-2}}, \qquad (7)$$

where

$$A = \frac{3\kappa_\gamma M_{\rm ej}}{4\pi v_{\rm ej}^2} \qquad (8)$$

is the leakage parameter and κ_γ is the gamma-ray opacity of the ejecta.

The radioactive power from the decay of ^{56}Ni is given by

$$L_{\rm ra} = f_{\rm Ni} M_{\rm ej} (L_{^{56}{\rm Ni}} e^{-t/t_{^{56}{\rm Ni}}} + L_{^{56}{\rm Co}} e^{-t/t_{^{56}{\rm Co}}}), \qquad (9)$$

where $f_{\rm Ni}$ is the nickel fraction of the ejecta, $L_{^{56}{\rm Ni}} = 6.45 \times 10^{43}$ erg s^{-1} $M_\odot^{-1}$ and $L_{^{56}{\rm Co}} = 1.45 \times 10^{43}$ erg s^{-1} $M_\odot^{-1}$ are the decay luminosities of ^{56}Ni and ^{56}Co, and $t_{^{56}{\rm Ni}} = 8.8$ d and $t_{^{56}{\rm Co}} = 111.3$ d are the decay time-scales for ^{56}Ni and ^{56}Co (Nadyozhin 1994). The inclusion of $L_{\rm ra}$ here allows our model to simplify to an Arnett (1982) model for low $L_{\rm SD}$.

The dynamical evolution of the ejecta is given by (Sarin et al. 2022)

$$\frac{{\rm d}v_{\rm ej}}{{\rm d}t} = \frac{c^2 \mathcal{P}({\rm d}\mathcal{V}/{\rm d}t)}{M_{\rm ej} v_{\rm ej}^3}, \qquad (10)$$

where

$$\mathcal{V} = \frac{4}{3}\pi R_{\rm ej}^3, \qquad (11)$$

$$\frac{{\rm d}\mathcal{V}}{{\rm d}t} = 4\pi R_{\rm ej}^2 v_{\rm ej}, \qquad (12)$$

$$\mathcal{P} = \frac{E_{\rm int}}{3\mathcal{V}}. \qquad (13)$$

Substituting these into equation (10) gives

$$\frac{{\rm d}v_{\rm ej}}{{\rm d}t} = \frac{c^2 E_{\rm int}}{M_{\rm ej} R_{\rm ej} v_{\rm ej}^2}. \qquad (14)$$

The initial ejecta velocity is set by

$$v_{\rm ej,0} = \sqrt{\frac{2E_{\rm SN}}{M_{\rm ej}}}, \qquad (15)$$

where $E_{\rm SN}$ is the supernova explosion energy.

The bolometric radiated luminosity is (Kasen & Bildsten 2010; Kotera, Phinney & Olinto 2013)

$$L_{\rm bol} = \frac{E_{\rm int}c}{\tau R_{\rm ej}} = \frac{E_{\rm int}t}{t_{\rm dif}^2} \ (t \le t_\tau), \qquad (16)$$

$$= \frac{E_{\rm int}c}{R_{\rm ej}}, \ (t > t_\tau), \qquad (17)$$

where

$$\tau = \frac{\kappa M_{\rm ej} R_{\rm ej}}{\mathcal{V}} \qquad (18)$$

is the optical depth of the ejecta, κ is the ejecta opacity,

$$t_{\rm dif} = \left(\frac{\tau R_{\rm ej} t}{c}\right)^{1/2} \qquad (19)$$

is the effective diffusion time, and $t_\tau > t_{\rm dif}$ is the time when $\tau = 1$.

Calculating the bolometric luminosity of the magnetar-driven transient [equations (16) and (17)] involves solving the evolution of the internal energy and dynamics [equations (6) and (14) respectively] using the input power sources [equations (3) and (9)]. The photospheric temperature is determined from the bolometric luminosity and ejecta radius until the temperature reaches the photospheric plateau temperature, as in Nicholl, Guillochon & Berger (2017b). This can be expressed as

$$T_{\rm phot}(t) = \begin{cases} \left(\frac{L_{\rm bol}(t)}{4\pi\sigma R_{\rm ej}^2}\right)^{1/4} & \text{for } \left(\frac{L_{\rm bol}(t)}{4\pi\sigma R_{\rm ej}^2}\right)^{1/4} > T_{\rm min}, \\ T_{\rm min} & \text{for } \left(\frac{L_{\rm bol}(t)}{4\pi\sigma R_{\rm ej}^2}\right)^{1/4} \le T_{\rm min} \end{cases} \qquad (20)$$

The spectral energy distribution (SED) of the transient is then calculated using the cutoff blackbody used in Nicholl, Guillochon & Berger (2017b), with $F_{\lambda < \lambda_{\rm cut}} = F_\lambda(\lambda/\lambda_{\rm cut})$ and $\lambda_{\rm cut} = 3000$ Å (Chomiuk et al. 2011; Nicholl et al. 2017a), but this can also be switched to a simple blackbody.

2.2 Parameters, priors, and implementation

The model presented above is implemented into the open-source electromagnetic transient fitting software package, REDBACK (Sarin et al. 2023). The input parameters for the model, their default priors, and the values used in Section 3 are listed in Table 1.

The range of the default priors can lead to magnetars with rotational energies greater than 10^{58} erg, which is unphysically high. When performing inference, the prior can be restricted to only sample parameters where $E_{\rm rot}$ is below a certain threshold. We recommend using this constraint to prevent unphysically high energies, and use a value of 10^{53} erg for the case studies presented in Section 4.

Table 1. The parameters and default priors for the generalized magnetar model, as well as the values used for the parameter exploration in Section 3. Priors are either uniform (U) or log-uniform (L).

Parameter	Definition	Units	Default prior	Section 3.1 value
L_0	Initial magnetar spin-down luminosity	erg s^{-1}	L[10^{40}, 10^{50}]	Varying
t_{SD}	Spin-down time	s	L[10^2, 10^8]	Varying
n	Magnetar braking index	–	U[1.5, 10]	3
f_{Ni}	Ejecta nickel mass fraction	–	L[10^{-3}, 1]	0
M_{ej}	Ejecta mass	$M_\odot$	L[10^{-2}, 1×10^2]	Varying
E_{SN}	Supernova explosion energy	erg	U[5×10^{50}, 2×10^{51}]	10^{51}
κ	Ejecta opacity	cm^2 g^{-1}	U[0.05, 0.2]	0.1
κ_γ	Ejecta gamma-ray opacity	cm^2 g^{-1}	L[10^{-4}, 10^4]	0.1
T_{min}	Photospheric plateau temperature	K	U[3×10^3, 10^4]	5000

Due to the acceleration of the ejecta from the PWN, v_{ej} is not constant and cannot be used as a free parameter, since it is coupled to both E_{SN} and L_{SD}. Velocity information from spectroscopy can be used to weight the results, although the velocity measured from absorption widths is not the same as the photospheric velocity which is not the same as the ejecta velocity (Arnett 1982), so we caution against this unless the velocities are well calibrated (e.g. Dessart et al. 2016).

Our model differs from others (e.g. Nicholl, Guillochon & Berger 2017b) in the choice of input parameters used to determine the magnetar luminosity. Previous models use the initial magnetar spin period P_0, dipole component of the pulsar magnetic field B, and neutron star mass M_{NS}; while we use L_0 and t_{SD} (and n, which is implicitly fixed to 3 in other models). The interpretation of braking index can be complicated due to the number of possible spin-down mechanisms, so users wanting to test specific mechanisms can swap different magnetar implementations due to the modular nature of the model and REDBACK. We note that as the magnetar luminosity for vacuum dipole spin-down can be determined from only L_0 and t_{SD} (see equation 3), using three parameters is unnecessary for parameter inference. Using these parameters also avoids assumptions such as the moment of inertia of the neutron star, which depends on the equation of state (EoS) (Lattimer & Schutz 2005) and can vary depending on the mass and spin period of the neutron star (Worley, Krastev & Li 2008). To recover parameters such as the magnetar spin period and magnetic field, one can use the scalings used in other models such as

$$L_0 = 2.0 \times 10^{47} P_{0,-3}^{-4} B_{14}^2, \tag{21}$$

$$t_{SD} = 1.3 \times 10^5 P_{0,-3}^2 B_{14}^{-2} \left(\frac{M_{NS}}{1.4 M_\odot} \right) \tag{22}$$

for transients consistent with $n = 3$, which assumes a neutron star with moment of inertia of $\sim 1.3 \times 10^{45}$ g cm^2 for a $1.4 M_\odot$ neutron star, which is consistent with the APR EoS (Akmal, Pandharipande & Ravenhall 1998) or MDI EoS with density independent nuclear symmetry energy (Das et al. 2003; Shetty, Yennello & Souliotis 2007), which both give neutron star radii $\sim 11.5 - 12$ km (Worley, Krastev & Li 2008). These scalings become more complicated for $n \neq 3$ (e.g. Shapiro & Teukolsky 1983), with other dependencies such as the ellipticity of the neutron star or bulk viscosity (depending on the spin-down processes involved), leaving it difficult to definitively recover a spin period or magnetic field with such simplified models.

3 RESULTS

We now explore the diversity of magnetar driven-supernovae for different initial conditions using the model derived in Section 2.

We assume the supernova explosion energy is 10^{51} erg, typical for a neutrino-driven explosion, and the supernova is entirely powered by magnetar energy after the initial explosion, with no contribution from ^{56}Ni. We fix both the ejecta optical opacity and gamma-ray opacity to 0.1 cm^2 g^{-1}. This optical opacity value is typical of stripped-envelope supernovae (Inserra et al. 2013; Kleiser & Kasen 2014) and the gamma-ray opacity will not affect the peak light-curve properties unless it is extremely low, so we use the same value for both opacities here for simplicity. We also fix the photospheric plateau temperature to 5000 K, which is typical for SLSNe (Nicholl, Guillochon & Berger 2017b) and SNe Ic-BL (Taddia et al. 2019), although slightly lower than the temperature of 6000 K suggested by Nicholl, Guillochon & Berger (2017b), which corresponds to the recombination temperature of O II; ultimately, this temperature discrepancy will have no impact on the peak light-curve properties in most cases, and will only affect the light curve at late times.

First, we show the diversity of supernovae that can be produced using this model in Section 3.1. To compare with previously derived results, we assume vacuum dipole spin-down and use equations (21) and (22) with a $1.4 M_\odot$ neutron star to express our initial conditions in terms of P_0 and B; the mapping between (L_0, t_{SD}) and (P_0, B) is shown in Fig. 1. Then we show the effect of changing braking index in Section 3.2.

3.1 Energetics, time-scales, and observables

We first see if our model can reproduce typical observables for the observed populations of SLSNe and SNe Ic-BL. SLSNe at optical light-curve peak typically have g-band absolute magnitudes $-23 < M_g < -20$, with most brighter than -21; spectroscopically determined photospheric velocities of $\sim 10\,000–15\,000$ km s^{-1}; rise times of 10–70 d; and $g - r$ of $-0.3–0.3$ (Chen et al. 2023a). SNe Ic-BL at optical light-curve peak typically have r-band absolute magnitudes around $-20 < M_r < -18$, with most fainter than -19; spectroscopically determined photospheric velocities of $\sim 15\,000–30\,000$ km s^{-1} (Modjaz et al. 2016); rise times of 5–20 d; and $g - r$ of 0–0.5 (Taddia et al. 2019). The inferred ejecta masses of typical SLSNe and SNe Ic-BL are both around $5 M_\odot$ (Taddia et al. 2019; Chen et al. 2023b), and SLSNe show a negative correlation between initial spin period and ejecta mass (Blanchard et al. 2020). We also compare our results to the 2D radiation-hydrodynamic simulations of Suzuki & Maeda (2021), who presented models with $L_0 = 10^{46}$ erg s^{-1} (L46 models) and $L_0 = 10^{48}$ erg s^{-1} (L48 models) and total magnetar rotational energies of 1, 3, and 10×10^{51} erg.

Several inefficiencies can prevent all the magnetar spin-down luminosity from eventually being emitted as supernova luminosity. Some fraction [ξ from equation (6)] will escape without interacting
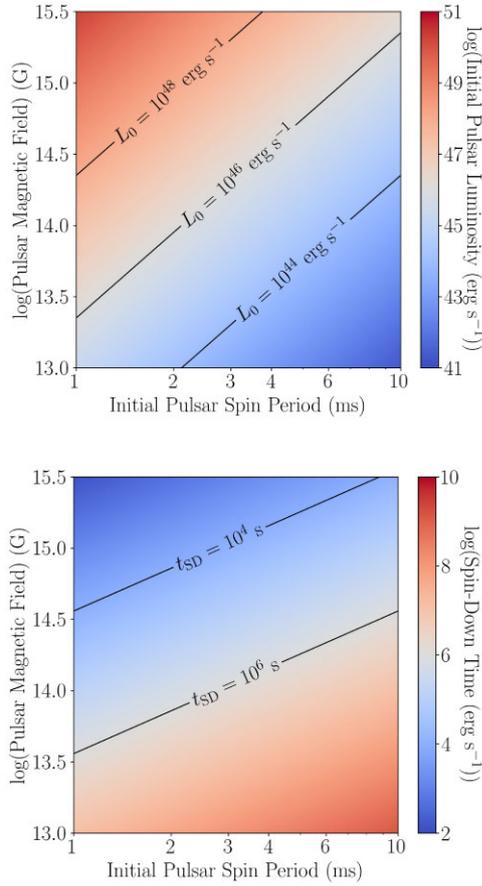
Figure 1. Initial pulsar luminosities L_0 (top) and spin-down times $t_{\rm SD}$ (bottom) for different initial pulsar rotation periods and magnetic fields.

with the ejecta at all, and possibly be detected as non-thermal x-rays or gamma rays. Some fraction of the energy will also accelerate the ejecta instead of thermalizing and being re-emitted, which will affect both the supernova luminosity and peak time-scale; this fraction can be determined by the ratio of the spin-down time and the diffusion time (Suzuki & Maeda 2021; Sarin et al. 2022).

Fig. 2 shows the ratio of the final supernova kinetic and radiated energies for various magnetic fields and ejecta masses for spin periods of 1 ms (close to the mass shedding limit for neutron stars; Watts et al. 2016) and 3 ms (where the spin-down luminosity and explosion energy can become comparable), and for various magnetic fields and spin periods for an ejecta mass of $10\,M_\odot$, the same ejecta mass as Suzuki & Maeda (2021). The energy ratio $E_{\rm kin}/E_{\rm rad}$ does correlate strongly with $\zeta = t_{\rm SD}/t_{\rm dif}$ up to large ejecta mass for low spin periods, although as spin period increases, the correlation gets weaker as the behaviour of the energy ratio changes; this is due to the total amount of energy injected by the magnetar prior to the diffusion time decreasing below the explosion energy, meaning that the ejecta dynamics are no longer primarily determined by the magnetar spin-down energy. There is a small region of the parameter space at low spin period, magnetic field, and ejecta mass where the radiated energy can surpass the kinetic energy. However, for most of the parameter space this ratio is between 1 and 100. Typical supernovae have $E_{\rm kin}/E_{\rm rad} = 10^{51}$ erg/10^{49} erg $= 100$, but without a contribution from ^{56}Ni this ratio can go much higher. Suzuki & Maeda (2021) find $E_{\rm kin}/E_{\rm rad}$ to be lower than we do in their 2D simulations by a factor of ~ 2–10 depending on the model. However, they also find that multi-dimensional effects cause the supernova to be more luminous compared to 1D models at early times due to hot bubble breakout in the ejecta.

Fig. 3 shows the peak time-scale of the bolometric luminosity and the final ejecta velocity over the same parameter grid as Fig. 2. The trends match our theoretical expectations, as P_0 increases, the total energy of the system decreases, causing the ejecta velocity to decrease and the peak time-scale to increase. Conversely, as B increases, the spin-down time decreases, causing the ejecta velocity to increase and the peak time-scale to decrease. Finally, as $M_{\rm ej}$ increases, the diffusion time increases, causing the ejecta velocity to decrease and the peak time-scale to increase. The final ejecta velocity is largely insensitive to the magnetic field strength above a certain field threshold despite a change in peak time-scale. This is a product of the coupling of dynamical evolution of the ejecta to the magnetar's rotational energy, as the final velocity is reached earlier in the supernova evolution for higher magnetic field (due to their shorter spin-down time-scale). For a magnetar with rotation period of 1 ms, a magnetic field of $> 10^{15}$ is needed to reduce the peak time-scale below 10 d, even at an ejecta mass of $1\,M_\odot$, meaning that the fastest SNe Ic-BL likely require both an ejecta mass below $1\,M_\odot$ and a magnetar spinning at close to breakup speeds. Time-scales of >20 d require ejecta masses below $5\,M_\odot$, meaning that our model
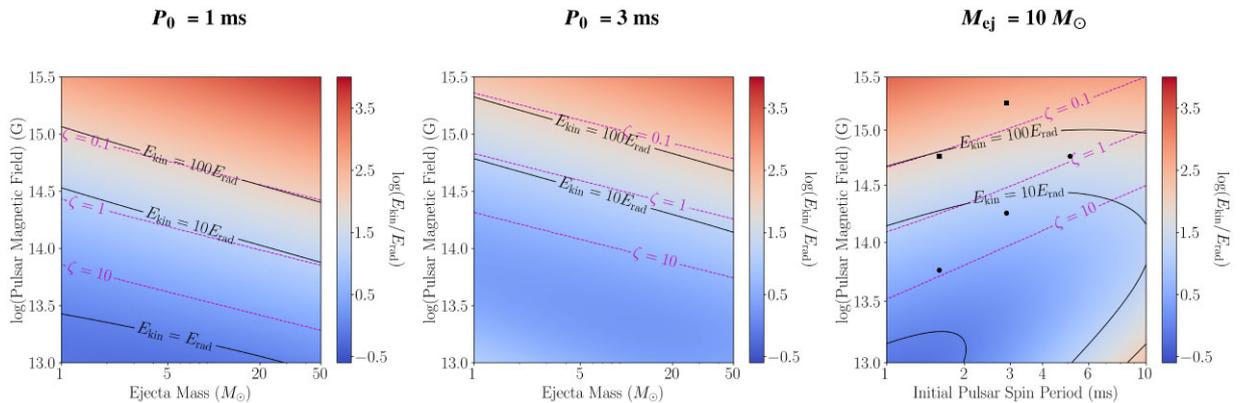

Figure 2. Ratio of kinetic to radiated energy for supernovae with varying ejecta mass and $P_0 = 1$ ms (left) and $P_0 = 3$ ms (middle) and with varying spin period and $M_{\rm ej} = 10M_\odot$ (right). The solid black lines indicate contours of constant $E_{\rm kin}/E_{\rm rad}$ (1,10, and 100), while the dashed magenta lines indicate contours of constant $\zeta = t_{\rm SD}/t_{\rm dif}$ (0.1, 1, and 10). The black symbols indicate the parameters used in Suzuki & Maeda (2021), with the circles representing the L46 models and the squares representing the L48 models.
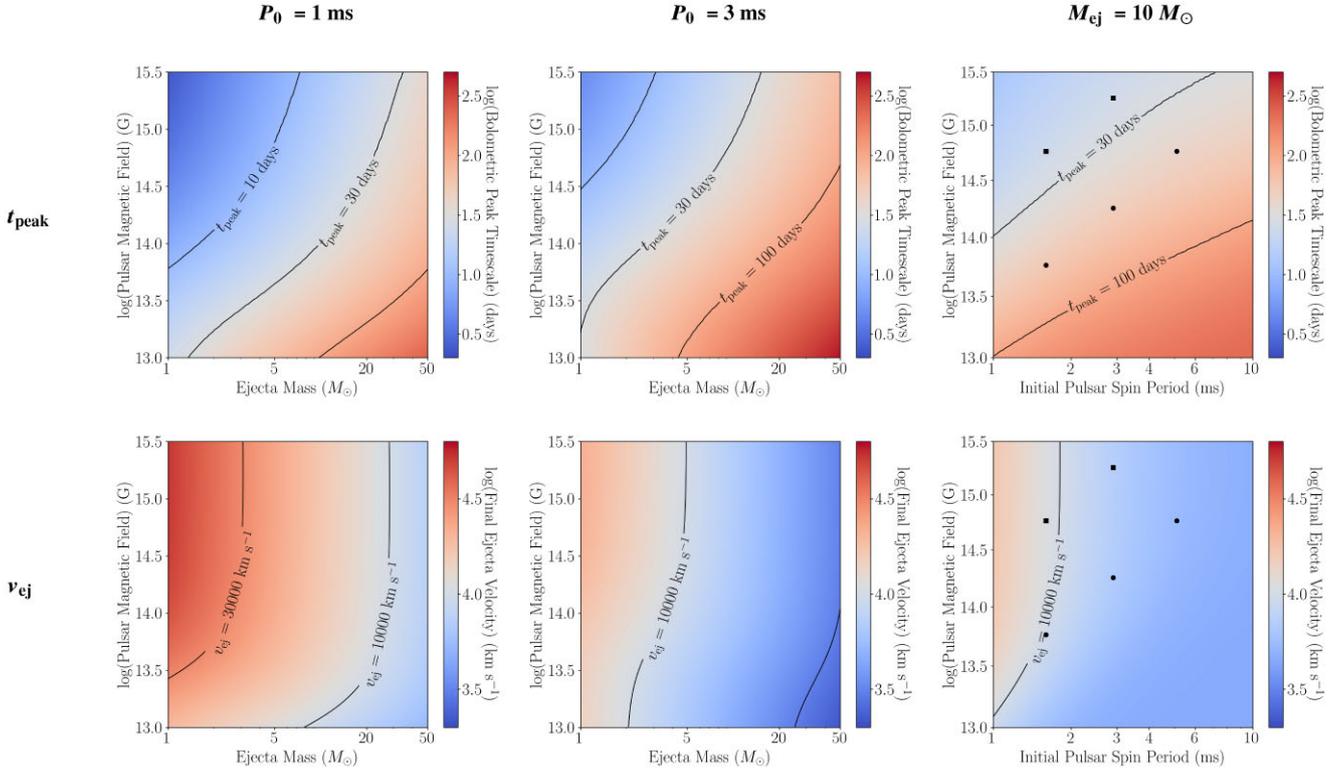
Figure 3. Bolometric peak time-scale t_{peak} (top) and final ejecta velocity v_{ej} (bottom) for supernovae with varying ejecta mass and $P_0 = 1$ ms (left) and $P_0 = 3$ ms (middle) and with varying spin period and $M_{ej} = 10M_\odot$ (right). The black lines indicate notable values of t_{peak} (10, 30, and 100 d) and v_{ej} (3000, 10 000, and 30 000 km s^{-1}). The black symbols indicate the parameters used in Suzuki & Maeda (2021), with the circles representing the L46 models and the squares representing the L48 models.

will likely estimate a lower ejecta mass for SNe Ic-BL than Taddia et al. (2019). Time-scales and ejecta velocities typical of SLSNe can be reproduced over a large portion of the parameter space. However, a higher ejecta mass is required for faster spinning magnetars to keep the velocities below that of SNe Ic-BL. In contrast, a low ejecta mass is required for faster spinning magnetars to keep the time-scales below ~ 100 d and the velocities higher than $\sim 10\,000$ km s^{-1}, providing some phenomenological justification for the mass–spin correlation found by Blanchard et al. (2020). Suzuki & Maeda (2021) find faster time-scales compared to us in the L46 2D simulations, but similar time-scales in their 1D simulations, and an average ejecta velocity that is roughly consistent with our model.

Fig. 4 shows the peak g-band absolute magnitude and peak $g - r$ colour over the same parameter grid. We find a portion of parameter space for low spin period, ejecta mass, and magnetic field which produces a transient more luminous than any previously observed superluminous supernova. However, it is unlikely such a combination (particularly low spin period and magnetic fields) can be conceived as magnetic-field amplification mechanisms such as the magnetorotational instability or Kelvin-Helmholtz instability likely amplify most typical progenitor fields to larger poloidal fields than seen in this parameter space (e.g. Reboul-Salze et al. 2021), meanwhile, the stability of magnetic-field configurations in this part of the parameter space is also questionable (e.g. Braithwaite 2009) and so magnetars in this parameter space may never materialize. We note that as we do not track gravitational-wave losses, the newly born magnetar could potentially spin-down rapidly through gravitational-wave radiation (Sarin & Lasky 2021) in this parameter space, depleting the energy reservoir to power such a luminous transient. To compound this all further, it is unknown whether stellar

explosions with such small ejecta masses could harbour magnetars that are rapidly rotating but have quite weak poloidal fields in the first place. The parameter space between $M_g = -21$ and $M_g = -23$, where SLSN are, shifts to lower masses for higher spin periods, where the parameter space around $M_g = -19$, where most SNe Ic-BL are, require either a large ejecta mass ($\gtrsim 5M_\odot$), higher spin period, or extremely high magnetic field. The parameter space where $g - r < 0$ mostly overlaps with the $M_g < -21$ region, showing that most SLSNe should have $-0.5 < g - r < 0$ at peak, which is broadly consistent with observations (Chen et al. 2023a). Suzuki & Maeda (2021) only present bolometric results, but find an increase in peak bolometric magnitude of ~ 5 in 2D simulations and ~ 4 in 1D simulations between the most and least energetic L46 models, while we find an increase of ~ 4 in g-band magnitude over the same parameter difference. The magnitudes are also roughly consistent with the analytical model presented in Kashiyama et al. (2016). The energy ratios from Fig. 2 roughly coincide with the peak M_g for the parameter region where $\zeta \lesssim 1$, but as the spin-down time increases, a larger fraction of the emission is emitted post-peak. The $g - r$ colours show similar behaviour to M_g, but show less dependence on magnetic field. We speculate that this is because the peak time-scale is shorter, and thus the ejecta has had less time to cool.

3.2 Effect of varying braking index

Light-curve luminosity and morphology can vary significantly with variations in magnetar braking index. Fig. 5 shows the bolometric luminosity, absolute g-band magnitude, and absolute r-band magni-
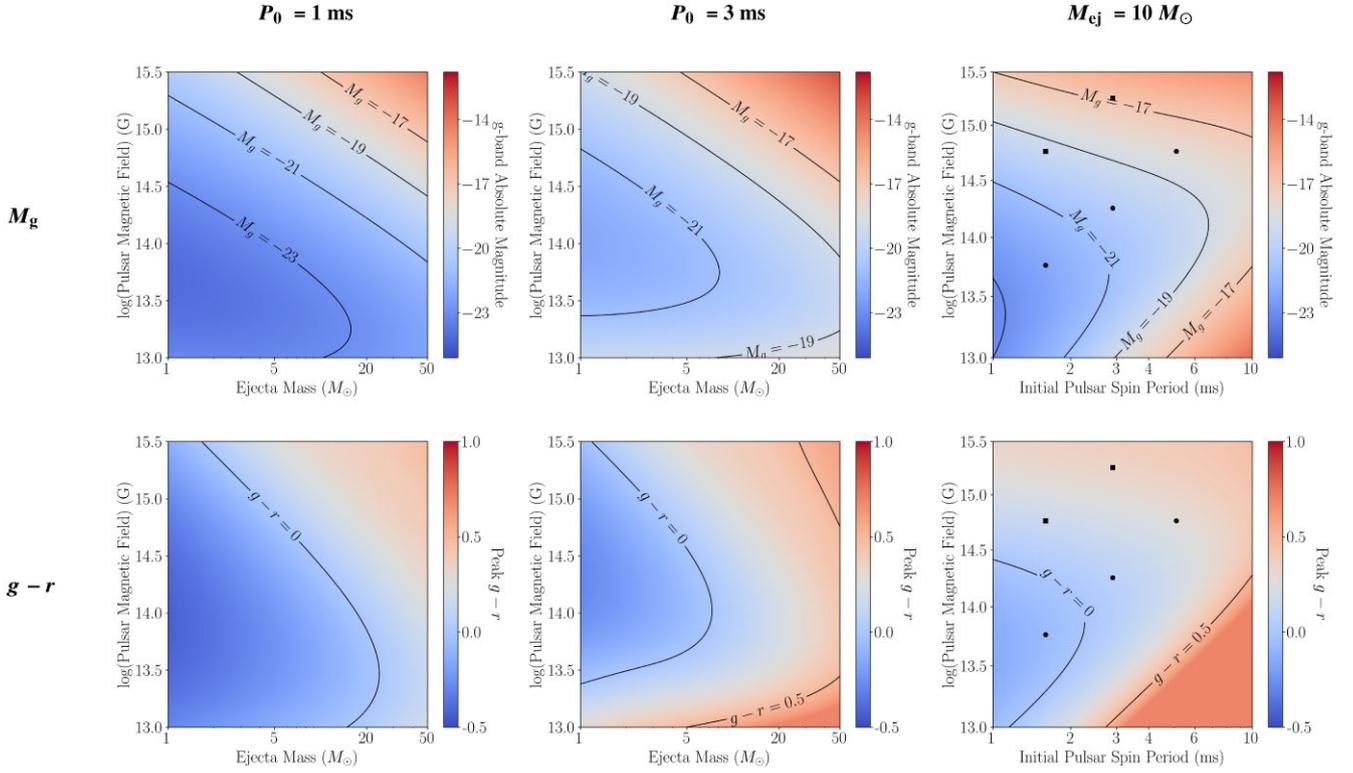
Figure 4. g-band absolute magnitude M_g (top) and $g - r$ colour (bottom) at peak for supernovae with varying ejecta mass and $P_0 = 1$ ms (left) and $P_0 = 3$ ms (middle) and with varying spin period and $M_{ej} = 10 M_\odot$ (right). The black lines indicate notable values of M_g (-17, -19, -21, and -23) and $g - r$ (0 and 0.5). The black symbols indicate the parameters used in Suzuki & Maeda (2021), with the circles representing the L46 models and the squares representing the L48 models.
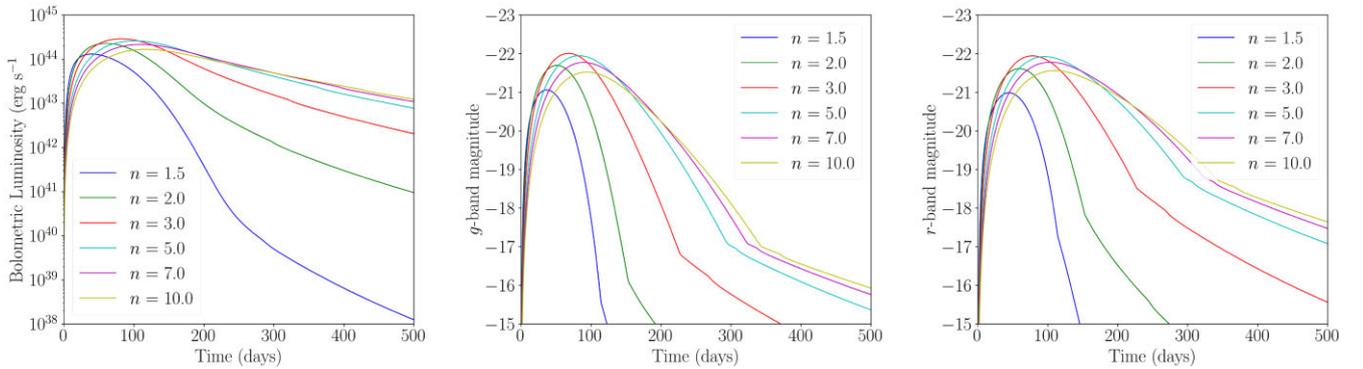
Figure 5. Bolometric luminosity (left), absolute g-band magnitude (middle), and absolute r-band magnitude (right) for several supernovae where only the braking index n is varied.

tude for several supernovae where only the braking index n is varied. The ejecta mass, spin-down time, and total rotational energy are fixed to $10 M_\odot$, 10^6 s, and 10^{52} erg, with initial magnetar luminosity calculated from equation (4); all other parameters are the same as in Section 3.1. The timing of the light-curve peak can vary by a factor of ~ 3 and late-time luminosities by orders of magnitude, with large n peaking later and having higher luminosities at later times, although the variation in late-time luminosity asymptotes as n increases due to the exponent in equation (3) asymptoting to -1. The peak luminosity can vary by ~ 1 mag and is highest for $n \approx 3$ in this case, although this is not true in general, and these numbers will vary depending on the energetics and diffusion time of the supernova. The requirement of constant rotational energy drives down L_0 (equation 4), leading

to less energy injected at early times and more at later times, which causes the peak luminosity to decreases at large n.

4 CASE STUDIES FOR INFERENCE

As a proof of concept, we perform inference on several different classes of supernovae to see if the model is flexible enough to recover sensible parameters for a variety of objects. First, we validate the model using a simulated SLSN. Then, we perform inference on SN 2015bn, an SLSN; SN 2007ru, a SN Ic-BL; ZTF20acigmel (better known as 'the Camel'), an FBOT; and iPTF14gqr, a USSN.

Inference is performed on multiband photometry using the open-source software package REDBACK (Sarin et al. 2023) with the
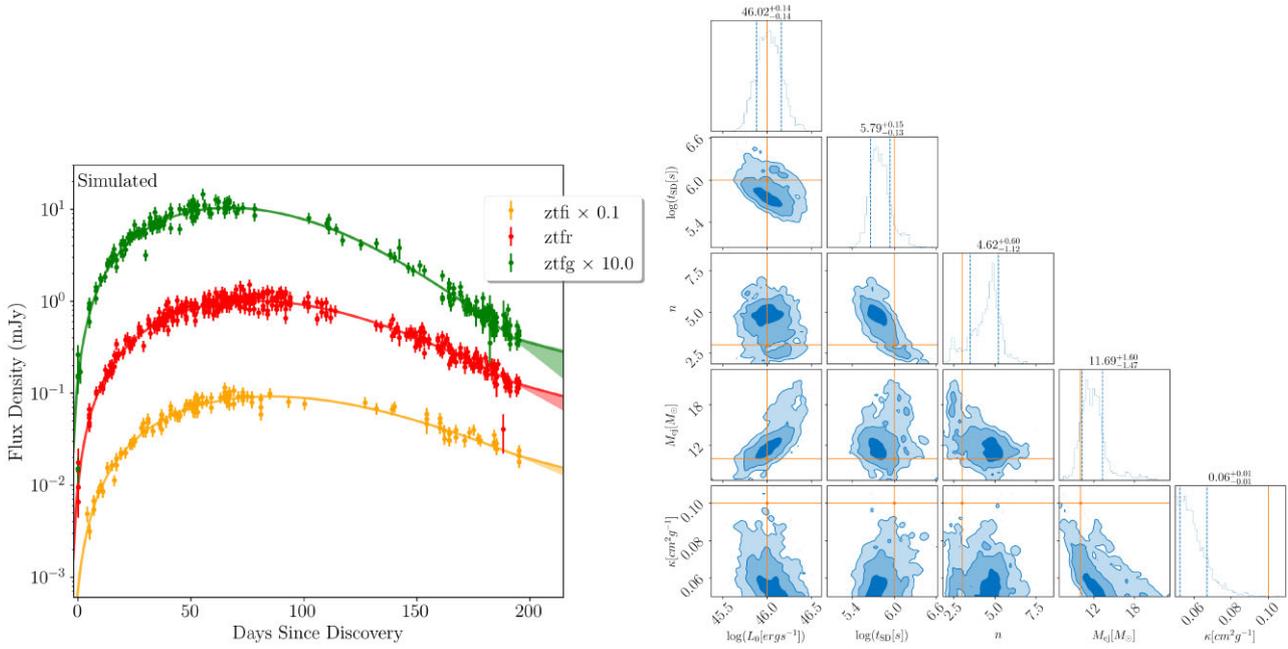
Figure 6. Fitted light curve (left) and posteriors of key parameters (right) for the simulated SLSN. The solid lines in the light-curve plot indicate the light curve from the model with the highest likelihood, while the shaded area indicates the 90 per cent credible interval. The orange dots and lines in the posterior indicate the injected parameters.

DYNESTY sampler (Speagle 2020) implemented in BILBY (Ashton et al. 2019; Romero-Shaw et al. 2020). We sample with a Gaussian likelihood and an additional white noise term, and sample in flux density rather than magnitude. We use the default priors in all cases (shown in Table 1) except for the explosion energy of iPTF14gqr, where the lower limit is reduced to 5×10^{48} erg to capture the lower expected explosion energies of USSNe (Suwa et al. 2015), and the plateau temperature of ZTF20acigmel, where the observed photospheric temperature stayed at $\sim 20\,000$ K for the entire time it was detectable in optical/UV (Perley et al. 2021). We also sample the unknown explosion time with a uniform prior of up to 100 d before the first observation and an extinction term A_V with a uniform prior between 0 and 2, and use a constraint that the total rotational energy of the magnetar $E_{\rm rot} \lesssim 10^{53}$ erg.

The fitted light curve and corner plot for the simulated SN are shown in Fig. 6, the fitted light curves for the other SNe are shown in Fig. 7, the input parameters for the simulated SN and recovered parameters for each SN are shown in Table 2, and the corner plots for each SNe are shown in Appendix A.

4.1 Validation on a simulated supernova

To test if the model could recover parameters correctly, we simulated an SLSN with $L_0 = 10^{46}$ erg s^{-1}, $t_{\rm SD} = 10^6$ s, $n = 3$, $M_{\rm ej} = 10\,{\rm M}_\odot$, and $\kappa = 0.1$ cm^2 g^{-1}, with the other parameters the same as in Section 3. The supernova was placed at redshift $z = 0.1$ and data were generated using the REDBACK simulation workflow as observed by ZTF in g, r, and i band for the first 200 d post explosion.

The light curve (Fig. 6, left) is fit well by the model throughout its evolution. In the 1D posteriors, only L_0 is recovered to within 1σ, while $t_{\rm SD}$, n, and $M_{\rm ej}$, are recovered to just outside 1σ and κ is not recovered well at all. In the 2D posteriors, every parameter is recovered to within 2σ except for the n - $M_{\rm ej}$ posterior and anything involving κ. The correlations between L_0, $t_{\rm SD}$, and n also suggests

that the rotational energy of the magnetar is well constrained to $\sim 10^{52}$ erg, i.e. the injected value. The correlation between $M_{\rm ej}$ and κ is the main reason they are outside the 1σ error region in the 1D posteriors. n also shows an anticorrelation with κ_γ (see Fig. A1), showing that the effect of lowering the braking index can be mimicked in some cases by incomplete gamma-ray thermalization, although this degeneracy can likely be broken by acquiring data at later times. This result shows the importance of understanding the various opacities of different types of supernovae as well as the necessity of reporting inferred opacity values.

4.2 SN 2015bn

SN 2015bn is an SLSN-I at $z = 0.1136$ that was first discovered by the Catalina Sky Survey on 2014 December 23. It peaked at 79 rest-frame days post discovery, which made it one of the slowest evolving SLSNe at the time, and had peak magnitudes of $M_g = -22.0 \pm 0.08$ mag (AB) and $M_U = -23.07 \pm 0.09$ mag (Vega), making it one of the most luminous as well (Nicholl et al. 2016a). Since then, it has been followed-up extensively in optical/UV/NIR, with photometry and spectroscopy (Nicholl et al. 2016a, b, 2018), and polarimetry (Inserra et al. 2016; Leloudas et al. 2017), and well as in radio (Nicholl et al. 2018; Eftekhari et al. 2021; Murase et al. 2021) and X-rays (Inserra et al. 2017; Bhirombhakdi et al. 2018). SN 2015bn shows strong undulations in the light curve on a time-scale of 30–50 d (Nicholl et al. 2016a; Inserra et al. 2017), and was detectable in optical/UV for more than 1000 d (Nicholl et al. 2018), although the supernova has yet to be detected in either radio or X-rays.

We import the observational data (Nicholl et al. 2016a, b) from the Open Supernova Catalogue (Guillochon et al. 2017). Our model is able to fit the supernova peak very well in all bands but underestimates the IR bands in the post-peak photospheric phase and overestimates several bands after 300 d. The inferred rotational energy of the magnetar is $\sim 6 \times 10^{52}$ erg, which is close to the maximum rotational
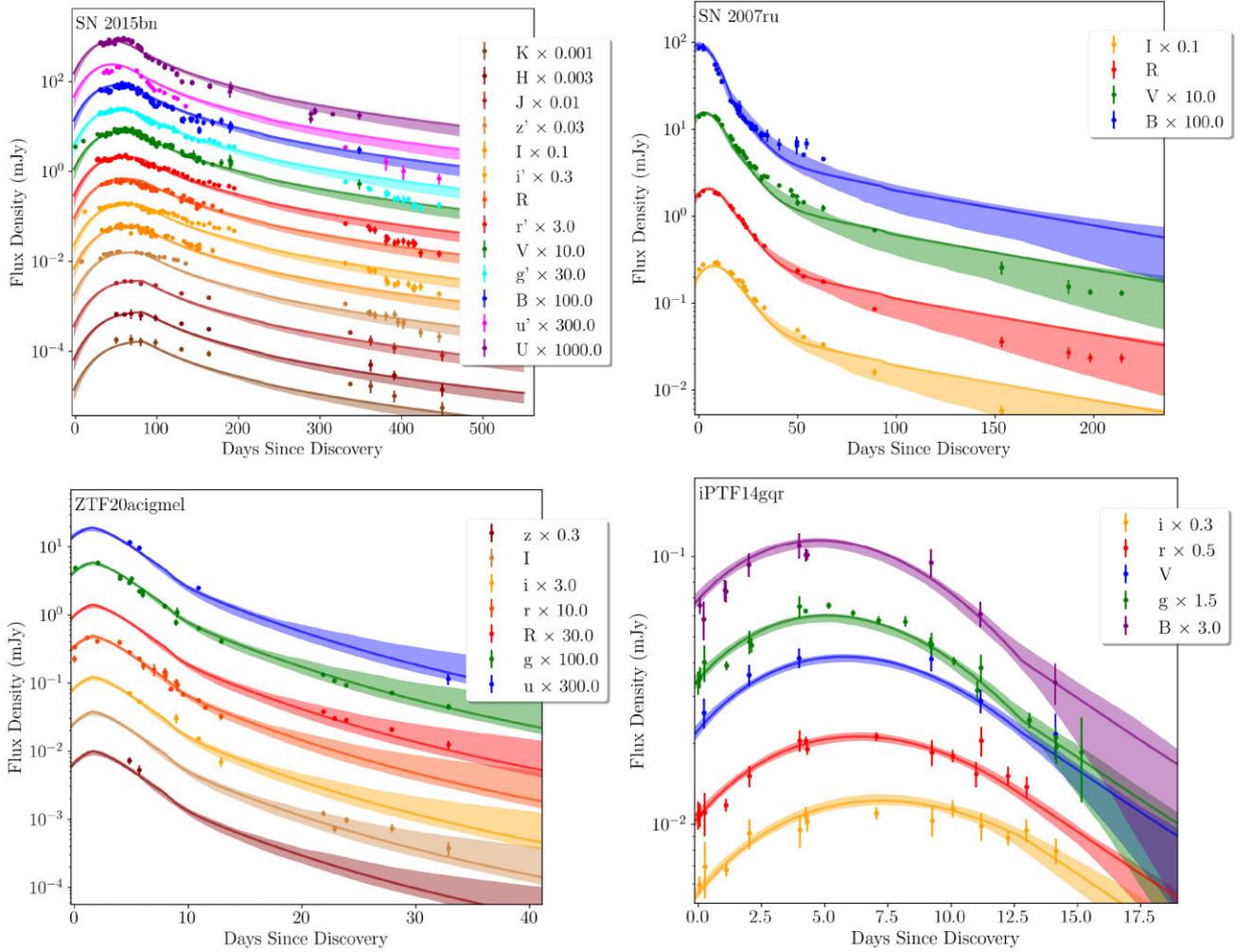
Figure 7. Fitted light curves for the four supernovae from our case studies. The solid lines indicate the light curve from the model with the highest likelihood, while the shaded area indicates the 90 per cent credible interval.

Table 2. Injected parameters for the simulated supernovae and median inferred parameter values and 1σ uncertainties for the simulated supernova and the four supernovae from the case studies.

Object	Supernova type	$\log(L_0)$ [erg s^{-1}]	$\log(t_{SD})$ [s]	n	M_{ej} [$M_\odot$]	κ [cm^2 g^{-1}]
Simulated (Injected)	–	46.0	6.0	3.0	10.0	0.1
Simulated (Recovered)	–	$46.02^{+0.14}_{-0.14}$	$5.79^{+0.15}_{-0.13}$	$4.62^{+0.60}_{-1.12}$	$11.69^{+1.60}_{-1.47}$	$0.06^{+0.01}_{-0.01}$
SN2015bn	SLSN	$44.81^{+0.04}_{-0.03}$	$7.54^{+0.20}_{-0.21}$	$6.28^{+2.43}_{-2.19}$	$6.05^{+0.59}_{-0.58}$	$0.05^{+0.00}_{-0.00}$
SN2007ru	Ic-BL	$46.27^{+0.97}_{-1.02}$	$3.31^{+0.78}_{-0.75}$	$5.24^{+1.18}_{-1.09}$	$1.48^{+0.35}_{-0.33}$	$0.06^{+0.02}_{-0.01}$
ZTF20acigmel	FBOT	$46.15^{+0.66}_{-0.68}$	$4.38^{+0.71}_{-0.49}$	$7.18^{+1.53}_{-3.54}$	$0.20^{+0.04}_{-0.05}$	$0.07^{+0.04}_{-0.02}$
iPTF14gqr	USSN	$43.31^{+0.27}_{-0.23}$	$5.81^{+0.32}_{-0.35}$	$4.37^{+2.14}_{-1.49}$	$0.15^{+0.07}_{-0.04}$	$0.16^{+0.03}_{-0.02}$

energy that can be extracted from a newborn magnetar. The gamma-ray opacity we find is around $10^{-2.4}$ cm^2 g^{-1}, which is consistent with Vurm & Metzger (2021) at around 200–300 d, when leakage starts to become noticeable. The magnetar also shows a large spread in inferred braking indices, but excludes $n = 3$ at $\gtrsim 95$ per cent confidence, meaning the vacuum dipole is not a good approximation for this object. Using equations (1) and (4) to infer the spin period, assuming a 1.4 $M_\odot$ neutron star with the same equation of state as Nicholl, Guillochon & Berger (2017b), gives $P_0 \approx 0.7$ ms, extremely close to the mass-shedding limit.

Comparing to the results of Nicholl, Guillochon & Berger (2017b) shows strong discrepancy between most inferred parameters. Using equations (4), (21), and (22) with parameters from Nicholl, Guillochon & Berger (2017b) show that they find a spin-down time-scale of ~ 105 d, much lower than our ~ 400 d, and a magnetar rotational energy of only $\sim 10^{52}$ erg, a factor of ~ 5 lower than recovered by our model. This is because the magnetar needs to supply both the radiated and kinetic energy of the supernova in our model, while in the Nicholl, Guillochon & Berger (2017b) model the ejecta velocity is input separately. We also recover a smaller ejecta mass of $\sim 6 M_\odot$,

compared to their $\sim 12\,M_\odot$, and a smaller opacity of ~ 0.05 cm^2 g^{-1}, compared to their ~ 0.19 cm^2 g^{-1}.

4.3 SN 2007ru

SN 2007ru is an SN Ic-BL at $z = 0.01546$ that was first discovered by the Himalayan Chandra Telescope on 2007 December 2 (Sahu et al. 2009). The peak magnitude of the supernova was $M_V \approx -19.06$ mag, one of the brighter SNe Ic-BL, and estimated rise time was 8 ± 3 d (Sahu et al. 2009). The photospheric velocity was estimated to be around 20 000 km s^{-1}. A nickel-powered model estimated the $M_{\rm ej}$ $\approx 1.3\,M_\odot$ and $M_{\rm Ni} \approx 0.4\,M_\odot$ (Sahu et al. 2009), while a previous magnetar-powered model estimated $P_0 \approx 2.30$ ms, $B \approx 6.2 \times 10^{15}$ G, and $M_{\rm ej} \approx 4.43\,M_\odot$ (Wang et al. 2016).

We import the observational data (Sahu et al. 2009) from the Open Supernova Catalogue (Guillochon et al. 2017). The model fits most of the data well in the optical and NIR. The magnetar energy is $\lesssim 10^{50}$ erg for this supernova, lower than the explosion energy, which dominates the dynamics here. This energy is also much lower than that estimated by Wang et al. (2016), and the spin-down time is a factor of ~ 10 larger. The ejecta mass we estimate is similar to the previous nickel-powered model, but lower than the previous magnetar-powered model. The opacity we recover is ~ 0.06 cm^2 g^{-1}, lower than the fixed value of 0.1 cm^2 g^{-1} in Wang et al. (2016). Finally, the braking index n is much higher than 3, and we can again reject vacuum dipole spin-down at $\gtrsim 95$ per cent confidence. Our posterior on the braking index is also consistent with the magnetar spin-down being dominated by gravitational-wave radiation (Sarin et al. 2018; Sarin, Lasky & Ashton 2020a). However we caution against strong conclusions based on the measurement of n due to our simplified treatment of the neutron star spin evolution.

4.4 ZTF20acigmel

AT2020xnd or ZTF20acigmel, the 'Camel', is an FBOT at z = 0.2433 that was first discovered by ZTF (Bellm et al. 2019) on 2020 October 12 (Perley et al. 2021). The peak magnitude was $M_{5000\text{Å}} \approx -20.6$ mag or $M_{3900\text{Å}} \approx -20.9$ mag, and estimated rise time was ~ 2 d (Perley et al. 2021). The photospheric radius is already receding at 7 d, and the photospheric temperature from 7 to 13 d is estimated to be 20 000 $\pm$ 2000 K. ZTF20acigmel was also found to be luminous in both radio (Ho et al. 2022) and X-rays (Bright et al. 2022).

We used the publicly available photometric data from Perley et al. (2021) for our fit. The model fits the data in all filters throughout the evolution of the object. The total rotational energy of the magnetar is around 10^{51} erg, comparable to the explosion energy. Using equations (1) and (4) to infer the spin period, again assuming a $1.4\,M_\odot$ neutron star with the same equation of state as Nicholl, Guillochon & Berger (2017b), gives $P_0 \approx 5$ ms. This value, as well as the ejecta mass, are consistent with values found for the FBOT distribution (Liu et al. 2022). The braking index has a wide distribution with two peaks, and is anticorrelated with the gamma-ray opacity, like with the simulated supernova. If the spin-down mechanism is vacuum dipole, then the gamma-ray opacity is likely $\gtrsim 1$ cm^2 g^{-1}, which can happen at late times for PWNe with magnetization similar to Galactic PWNe (Tanaka & Takahara 2010, 2013; Vurm & Metzger 2021). If the braking index is larger, then the gamma-ray opacity is smaller, and the magnetization must be lower, similar to SN 2015bn and SN 2017egm (Vurm & Metzger 2021). This can be potentially tested by observing non-thermal emission in the late phase.

4.5 iPTF14gqr

iPTF14gqr is a USSN at $z = 0.063$ that was first discovered by the intermediate Palomar Transient Factory (iPTF) (Law et al. 2009) on 2014 October 14. The supernova featured a bright first peak that faded within a day, followed by a more extended light curve that rises after about ~ 4 d. The first peak can be explained by shock cooling (De et al. 2018) and the second peak by either radioactivity (De et al. 2018) or a new born magnetar (Sawada, Kashiyama & Suwa 2022), although both peaks can also be explained by interaction alone (Khatami & Kasen 2023).

We used the publicly available photometric data from De et al. (2018), although we exclude all data points within one day post-explosion, since we only claim that the second peak could be magnetar powered. The model fits the data in all filters throughout the evolution of the object. The explosion energy, which has a wider prior to account for the low explosion energy of USSNe, is constrained to $\sim 6 \times 10^{49}$ erg, while the total magnetar rotational energy is $\sim 2 \times 10^{49}$ erg. The braking index is not very well constrained; although it is consistent with vacuum dipole to within error. The median spin-down time of ≈ 7 d is slightly lower than that found by Sawada, Kashiyama & Suwa (2022), although our magnetar energy is a factor of ~ 5 higher; this is likely because our explosion energy is smaller. The ejecta mass we derive is also consistent with estimates by both De et al. (2018) and Sawada, Kashiyama & Suwa (2022).

5 DISCUSSION AND SUMMARY

As shown by both the exploration of the parameter space (Section 3) and the case studies (Section 4), the model presented here is incredibly versatile. Three of the four case studies had previously been fit by a magnetar model (Wang et al. 2016; Nicholl, Guillochon & Berger 2017b; Sawada, Kashiyama & Suwa 2022), but each of these studies used a different model with different assumptions to model a particular supernova or class of supernovae. A versatile model allows comparisons of different populations to be done self-consistently and determine what model variations manifest in vastly different types of supernovae, as well as probe whether a continuum between these sources could exist or whether there are multiple distinct classes.

Much of the flexibility of our model comes from self-consistent dynamical evolution of the ejecta, while the addition of magnetar braking index as a parameter allows for some possible insight into the spin-down mechanism of the newborn millisecond magnetar. While inferring the spin-down mechanism for any particular supernova is difficult due to the number of possible mechanisms that could be in effect, we can constrain this parameter at a population level and see if different classes have evidence for different spin-down mechanisms. Fig. 8 (top) shows the posterior probability distribution of braking index for the four case study supernova. As mentioned above, $n = 3$ is rejected for SN 2015bn and SN 2007ru at > 95 per cent confidence; SN 2007ru shows a posterior that is roughly Gaussian while SN 2015bn shows a posterior that is roughly uniform at $n \gtrsim 4$. ZTF20acigmel and iPTF14gqr both show non-Gaussianity in their posteriors as well; the Camel has a double peaked distribution due to the degeneracy with gamma-ray opacity, while iPTF14gqr has a tail at high n but peaks very close to $n = 3$. While making definitive statements about spin-down mechanisms will require a much larger sample, this small sample already shows diversity in their inferred braking index, highlighting a potential interesting question for future studies.

All the objects studied in Section 4, including the simulated supernova, show a strong negative correlation between L_0 and $t_{\rm SD}$.
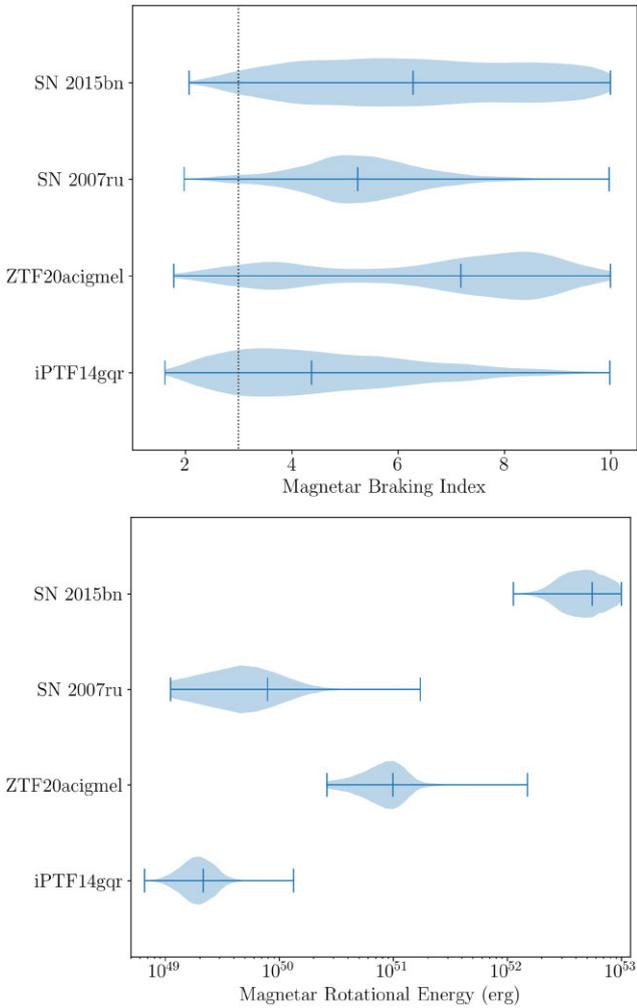
Figure 8. Posterior distributions of the magnetar braking index (top) and rotational energy (bottom) for the four supernovae from our case studies. The median values are indicated by the solid blue vertical lines within the distribution. The black dashed line indicates vacuum dipole spin-down ($n = 3$).

This shows that the magnetar rotational energy E_{rot}, and thus the total energy budget of the supernova, can be constrained for these objects to within an order of magnitude (see Fig. 8, bottom). The ejecta masses were all found to be similar to previous studies, except for SN 2015bn, and the spin-down times were found to differ for all models, usually by a factor of ~ 3–10. The magnitude of these discrepancies seems to vary depending on the supernova, and a large-scale sample study on supernovae that have been previously characterized by a magnetar model (e.g. Chen et al. 2023b) is necessary to characterize the systematic difference between our model and previous models.

Each magnetar-driven transient model (e.g. Yu, Zhang & Gao 2013; Kashiyama et al. 2016; Wang et al. 2016; Nicholl, Guillochon & Berger 2017b; Sarin et al. 2022; Sawada, Kashiyama & Suwa 2022) has slight differences in assumptions. All of these models assume vacuum dipole spin-down, although Kashiyama et al. (2016) and Sarin et al. (2022) also add a spin-down component for gravitational waves from magnetic deformation. For gamma-ray thermalization, Yu, Zhang & Gao (2013) uses a constant gamma-ray thermalization efficiency, Kashiyama et al. (2016) models the non-thermal emission and deposition using several additional free parameters, while Wang et al. (2016), Nicholl, Guillochon & Berger

(2017b), and Sarin et al. (2022) use the same prescription we do. Nicholl, Guillochon & Berger (2017b) and Sawada, Kashiyama & Suwa (2022) do not treat the effect of the magnetar on the ejecta dynamics, while Wang et al. (2016) uses a simplified treatment. The kilonova models (Yu, Zhang & Gao 2013; Sarin et al. 2022) have different radioactive heating rates due to the r-process material in the ejecta, while the other supernova models (Kashiyama et al. 2016; Wang et al. 2016; Nicholl, Guillochon & Berger 2017b; Sawada, Kashiyama & Suwa 2022) are non-relativistic and cannot be used for transients with exceptionally low ejecta masses and powerful magnetar engines. Finally, only Nicholl, Guillochon & Berger (2017b) and Sarin et al. (2022) were originally implemented into a publicly available Bayesian inference code (Guillochon et al. 2017; Sarin et al. 2023), although the Yu, Zhang & Gao (2013) model has also been implemented in REDBACK.

This model has a few caveats which may prevent it from properly describing certain transients. The first is that it is a one-zone, 1D model. This makes the treatment of the photospheric radius very simplified compared to real supernovae. Engine-driven supernovae also show hydrodynamic instabilities in multidimensional simulations (e.g. Chen, Woosley & Sukhbold 2016; Suzuki & Maeda 2017, 2019; Chen, Woosley & Whalen 2020; Suzuki & Maeda 2021) which can shred the inner ejecta, causing a decrease in the effective optical depth of the ejecta, as well as affecting the time-scale for non-thermal leakage. While our model can qualitatively produce the same behaviour as radiation hydrodynamic simulations, multidimensional effects cause the supernova peak to be earlier and more luminous. If the spin-down time-scale of the magnetar is smaller than the Kelvin-Helmholtz time-scale of the magnetar for neutrino emission $t_{KH,\nu} \lesssim 100$ s, then baryon loading on the magnetized wind via the neutrino-driven wind can be relevant (Thompson, Chang & Quataert 2004) and the magnetized wind can be collimated by anisotropic and hoop stress (Bucciantini et al. 2007, 2008) and form a jet (Kashiyama et al. 2016). This model also does not self-consistently track gravitational-wave emission and how it depletes the overall rotational energy reservoir. The model also has no way to explain the bumps and undulations that have recently found in a large number of SLSNe (Hosseinzadeh et al. 2022; Chen et al. 2023b), which have been explained by both circumstellar material (e.g. Chugai & Utrobin 2023; West et al. 2023) and magnetars (Chugai & Utrobin 2022; Moriya et al. 2022; Dong et al. 2023). The model we present can only explain a smooth light curve with minimal fine structure; however, this structure is likely connected to small mass ejections or binary interactions in the final few years of the life of the progenitor and may not be strongly connected to the power source of the supernova. Furthermore, the SED used in our model has a simplified treatment of line blanketing that is calibrated to SLSNe (Nicholl, Guillochon & Berger 2017b), and may not be accurate for other transients. Although it is possible to switch the SED to a blackbody if line blanketing is not expected to be strong, the SED is also not a good approximation deep into the nebular phase on the supernova, since the emission will start to be dominated by line emission instead of photospheric emission (e.g. Schulze et al. 2023).

Although the magnetar-driven supernova model is versatile enough to fit light curves of many different supernovae, the best way to determine whether a magnetar is really the power source is to compare the nebular spectra, polarization, and non-thermal emission from the supernovae with different models. Within the magnetar model, this emission is from the PWN or its interaction with the supernova ejecta. If the ejecta is optically thin, the synchrotron and inverse Compton emission from the PWN can leak through and be detected (Kotera, Phinney & Olinto 2013; Metzger et al. 2014;

Murase et al. 2015; Omand, Kashiyama & Murase 2018), while if the ejecta is optically thick, these photons will be absorbed and change the temperature and electronic state of the ejecta, both giving detectable signals (Chevalier & Fransson 1992; Omand, Kashiyama & Murase 2019; Omand & Jerkstrand 2023). However, interaction with circumstellar material can also produce non-thermal emission, polarization, and spectra with high ionization lines, therefore detailed modelling is necessary to make any strong conclusions.

In this work, we present a more flexible, inference-capable, publicly available model for the light curves of magnetar-driven supernovae. This model can be applied to any transient where the dominant power sources are either a magnetar or ^{56}Ni, as long as that energy release is roughly spherically symmetric. The main changes from previous models are the coupling of the magnetar energy injection to the kinetic energy of the supernova and the addition of the magnetar braking index as a free parameter, allowing the exploration of non-vacuum-dipole spin down. We show that the model can reproduce the basic properties on several phenomenologically different supernovae, and also fit four different types of supernovae, retrieving parameters consistent with works using separate models. This model will allow us to explore the full diversity of these supernovae, better characterize these supernovae from just their light curves, and make better predictions in future multiwavelength emission to better test the magnetar-driven scenario.

ACKNOWLEDGEMENTS

DATA AVAILABILITY

Light curve data for SN2015bn and SN2007ru was obtained from the Open Supernova Catalogue (Guillochon et al. 2017) using REDBACK. Light curve data for ZTF20acigmel and iPTF14gqr were downloaded from repositories released with the corresponding papers (De et al. 2018; Perley et al. 2021). The model is available for public use within REDBACK (Sarin et al. 2023).

REFERENCES

Akmal A., Pandharipande V. R., Ravenhall D. G., 1998, Phys. Rev. C, 58, 1804
Angus C. R. et al., 2016, MNRAS, 458, 84
Arnett W. D., 1980, ApJ, 237, 541
Arnett W. D., 1982, ApJ, 253, 785
Ashton G. et al., 2019, ApJS, 241, 27
Barkat Z., Rakavy G., Sack N., 1967, Phys. Rev. Lett., 18, 379
Bellm E. C. et al., 2019, PASP, 131, 018002
Bhirombhakdi K. et al., 2018, ApJ, 868, L32
Blanchard P. K. et al., 2019, ApJ, 872, 90
Blanchard P. K. et al., 2020, ApJ, 897, 114
Blandford R. D., Romani R. W., 1988, MNRAS, 234, 57P
Braithwaite J., 2009, MNRAS, 397, 763
Bright J. S. et al., 2022, ApJ, 926, 112
Bucciantini N. et al., 2007, MNRAS, 380, 1541
Bucciantini N. et al., 2008, MNRAS, 383, L25
Cano Z. et al., 2017, Adv. Astron., 2017, 8929054
Cappellaro E., 2022, Nuovo Cimento Riv. Ser., 45, 549
Chatzopoulos E., Wheeler J. C., 2012, ApJ, 760, 154
Chatzopoulos E. et al., 2013, ApJ, 773, 76

Chen W. C., Li X. D., 2006, A&A, 450, L1
Chen T. W. et al., 2015, MNRAS, 452, 1567
Chen K.-J., Woosley S. E., Sukhbold T., 2016, ApJ, 832, 73
Chen T.-W. et al., 2017, MNRAS, 470, 3566
Chen K.-J., Woosley S. E., Whalen D. J., 2020, ApJ, 893, 99
Chen T. W. et al., 2021, preprint (arXiv:2109.07942)
Chen Z. H. et al., 2023a, ApJ, 943, 41
Chen Z. H. et al., 2023b, ApJ, 943, 42
Chevalier R. A., Fransson C., 1992, ApJ, 395, 540
Chomiuk L. et al., 2011, ApJ, 743, 114
Chugai N. N., Utrobin V. P., 2022, MNRAS, 512, L71
Chugai N. N., Utrobin V. P., 2023, Astron. Lett., 49, 49
Contopoulos I., 2007, A&A, 466, 301
Contopoulos I., Spitkovsky A., 2006, ApJ, 643, 1139
Cutler C., Jones D. I., 2000, Phys. Rev. D, 63, 024002
Das C. B. et al., 2003, Phys. Rev. C, 67, 034611
De K. et al., 2018, Science, 362, 201
Dessart L. et al., 2016, MNRAS, 458, 1618
Dexter J., Kasen D., 2013, ApJ, 772, 30
Dong X.-F. et al., 2023, ApJ, 951, 61
Eftekhari T. et al., 2019, ApJ, 876, L10
Eftekhari T. et al., 2021, ApJ, 912, 21
Gaensler B. M., Slane P. O., 2006, ARA&A, 44, 17
Gal-Yam A., 2012, Science, 337, 927
Gal-Yam A. et al., 2009, Nature, 462, 624
Gendre B. et al., 2013, ApJ, 766, 30
Goldreich P., Julian W. H., 1969, ApJ, 157, 869
Guillochon J. et al., 2017, ApJ, 835, 64
Harding A. K., Contopoulos I., Kazanas D., 1999, ApJ, 525, L125
Hatsukade B. et al., 2021, ApJ, 911, L1
Heger A., Woosley S. E., 2002, ApJ, 567, 532
Heger A. et al., 2003, ApJ, 591, 288
Ho W. C. G., Lai D., 2000, ApJ, 543, 386
Ho A. Y. Q. et al., 2022, ApJ, 932, 116
Hosseinzadeh G. et al., 2022, ApJ, 933, 14
Inserra C. et al., 2013, ApJ, 770, 128
Inserra C. et al., 2016, ApJ, 831, 79
Inserra C. et al., 2017, MNRAS, 468, 4642
Ivezić Ž. et al., 2019, ApJ, 873, 111
Jerkstrand A. et al., 2017, ApJ, 835, 13
Jiang B., Jiang S., Ashley Villar V., 2020, Res. Notes Am. Astron. Soc., 4, 16
Kasen D., Bildsten L., 2010, ApJ, 717, 245
Kasen D., Metzger B. D., Bildsten L., 2016, ApJ, 821, 36
Kashiyama K. et al., 2016, ApJ, 818, 94
Khatami D., Kasen D., 2023, preprint (arXiv:2304.03360)
Kleiser I. K. W., Kasen D., 2014, MNRAS, 438, 318
Kotera K., Phinney E. S., Olinto A. V., 2013, MNRAS, 432, 3228
LSST Science Collaboration 2009, preprint (arXiv:0912.0201)
Lander S. K., Jones D. I., 2018, MNRAS, 481, 4169
Lander S. K., Jones D. I., 2020, MNRAS, 494, 4838
Lasky P. D. et al., 2017, ApJ, 843, L1
Lattimer J. M., Schutz B. F., 2005, ApJ, 629, 979
Law N. M. et al., 2009, PASP, 121, 1395
Law C. J. et al., 2019, ApJ, 886, 24
Lee C.-H., 2019, ApJ, 875, 121
Lee C.-H., 2020, Astron. Nachr., 341, 651
Leloudas G. et al., 2015a, MNRAS, 449, 917
Leloudas G. et al., 2015b, ApJ, 815, L10
Leloudas G. et al., 2017, ApJ, 837, L14
Levan A. J. et al., 2014, ApJ, 781, 13
Lin J. R., Zhang S. N., 2004, ApJ, 615, L133
Liu Y.-Q., Modjaz M., Bianco F. B., 2017, ApJ, 845, 85
Liu J.-F. et al., 2022, ApJ, 935, L34
Lunnan R. et al., 2014, ApJ, 787, 138
Lyne A. G. et al., 2015, MNRAS, 446, 857
MacFadyen A. I., Woosley S. E., 1999, ApJ, 524, 262
Metzger B. D., 2019, Living Rev. Relat., 23, 1
Metzger B. D. et al., 2014, MNRAS, 437, 703

Milisavljevic D. et al., 2013, ApJ, 770, L38
Modjaz M. et al., 2016, ApJ, 832, 108
Modjaz M., Gutiérrez C. P., Arcavi I., 2019, Nat. Astron., 3, 717
Mondal S. et al., 2020, MNRAS, 498, 3863
Moriya T. J., Nicholl M., Guillochon J., 2018, ApJ, 867, 113
Moriya T. J. et al., 2022, MNRAS, 513, 6210
Murase K. et al., 2015, ApJ, 805, 82
Murase K. et al., 2021, MNRAS, 508, 44
Nadyozhin D. K., 1994, ApJS, 92, 527
Nakauchi D. et al., 2013, ApJ, 778, 67
Nicholl M., 2021, Astron. Geophys., 62, 5
Nicholl M. et al., 2013, Nature, 502, 346
Nicholl M. et al., 2016a, ApJ, 826, 39
Nicholl M. et al., 2016b, ApJ, 828, L18
Nicholl M. et al., 2017a, ApJ, 835, L8
Nicholl M., Guillochon J., Berger E., 2017b, ApJ, 850, 55
Nicholl M. et al., 2018, ApJ, 866, L24
Omand C. M. B., Jerkstrand A., 2023, A&A, 673, A107
Omand C. M. B., Kashiyama K., Murase K., 2018, MNRAS, 474, 573
Omand C. M. B., Kashiyama K., Murase K., 2019, MNRAS, 484, 5468
Ørum S. V. et al., 2020, A&A, 643, A47
Ostriker J. P., Gunn J. E., 1969, ApJ, 157, 1395
Parthasarathy A. et al., 2020, MNRAS, 494, 2012
Pastorello A. et al., 2010, ApJ, 724, L16
Perley D. A. et al., 2021, MNRAS, 508, 5138
Pétri J., 2015, MNRAS, 450, 714
Poidevin F. et al., 2022, MNRAS, 511, 5948
Poidevin F. et al., 2023, MNRAS, 521, 5418
Pursiainen M. et al., 2022, A&A, 666, A30
Pursiainen M. et al., 2023, A&A, 674, A81
Reboul-Salze A., Guilet J., Raynaud R., Bugli M., 2021, A&A, 645, A109
Romero-Shaw I. M. et al., 2020, MNRAS, 499, 3295
Ruderman M., 2005, preprint (astro–ph/0510623)
Sahu D. K. et al., 2009, ApJ, 697, 676
Saito S. et al., 2020, ApJ, 894, 154
Sarin N., Lasky P. D., 2021, Gen. Relativ. Gravit., 53, 59
Sarin N. et al., 2018, Phys. Rev. D, 98, 043011
Sarin N., Lasky P. D., Ashton G., 2020a, Phys. Rev. D, 101, 063021
Sarin N., Lasky P. D., Ashton G., 2020b, MNRAS, 499, 5986
Sarin N. et al., 2022, MNRAS, 516, 4949
Sarin N. et al., 2023, preprint (arXiv:2308.12806)
Sawada R., Kashiyama K., Suwa Y., 2022, ApJ, 927, 223
Schulze S. et al., 2018, MNRAS, 473, 1258
Schulze S. et al., 2023, preprint (arXiv:2305.05796)

Shapiro S. L., Teukolsky S. A., 1983, Black Holes, White Dwarfs and Neutron Stars. The Physics of Compact Objects. Wiley-VCH, Weinheim
Shetty D. V., Yennello S. J., Souliotis G. A., 2007, Phys. Rev. C, 75, 034602
Smith N., 2014, ARA&A, 52, 487
Speagle J. S., 2020, MNRAS, 493, 3132
Stritzinger M., Moriya T., 2018, preprint (arXiv:1801.06643)
Stroh M. C. et al., 2021, ApJ, 923, L24
Sun L., Xiao L., Li G., 2022, MNRAS, 513, 4057
Suwa Y. et al., 2015, MNRAS, 454, 3073
Suzuki A., Maeda K., 2017, MNRAS, 466, 2633
Suzuki A., Maeda K., 2019, ApJ, 880, 150
Suzuki A., Maeda K., 2021, ApJ, 908, 217
Taddia F. et al., 2019, A&A, 621, A71
Tanaka S. J., Takahara F., 2010, ApJ, 715, 1248
Tanaka S. J., Takahara F., 2013, MNRAS, 429, 2945
Tanaka M. et al., 2017, ApJ, 837, 105
Thompson T. A., Chang P., Quataert E., 2004, ApJ, 611, 380
Tonry J. L., 2011, PASP, 123, 58
Tonry J. L. et al., 2018, PASP, 130, 064505
Villar V. A. et al., 2017, ApJ, 849, 70
Vurm I., Metzger B. D., 2021, ApJ, 917, 77
Wang S. Q. et al., 2015, ApJ, 799, 107
Wang L.-J. et al., 2016, ApJ, 831, 41
Watts A. L. et al., 2016, Rev. Mod. Phys., 88, 021001
West S. L. et al., 2023, A&A, 670, A7
Woosley S. E., 2010, ApJ, 719, L204
Woosley S. E., 2017, ApJ, 836, 244
Woosley S. E., Blinnikov S., Heger A., 2007, Nature, 450, 390
Worley A., Krastev P. G., Li B.-A., 2008, ApJ, 685, 390
Wu F., Xu R. X., Gil J., 2003, A&A, 409, 641
Xu R. X., Qiao G. J., 2001, ApJ, 561, L85
Yoshida T. et al., 2016, MNRAS, 457, 351
Yu Y.-W., Zhang B., Gao H., 2013, ApJ, 776, L40
Yue Y. L., Xu R. X., Zhu W. W., 2007, Adv. Space Res., 40, 1491
Zhang B., Mészáros P., 2001, ApJ, 552, L35

APPENDIX A: POSTERIORS FROM CASE STUDIES

Here we show the full posteriors for the simulated (Fig. A1) and real supernovae examined as case studies, SN 2015bn (Fig. A2), SN 2007ru (Fig. A3), ZTF20acigmel (Fig. A4), and iPTF14gqr (Fig. A5).
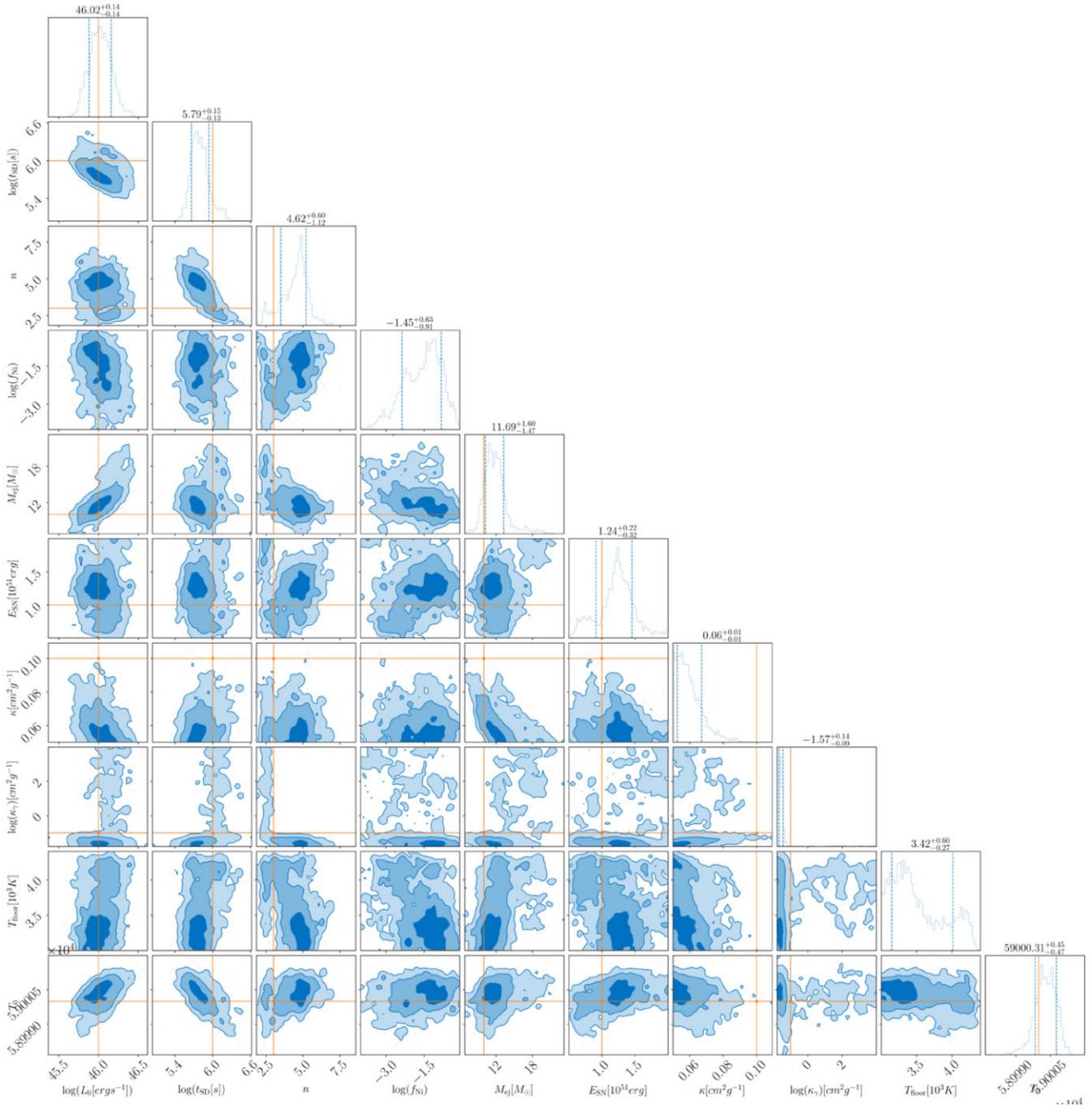
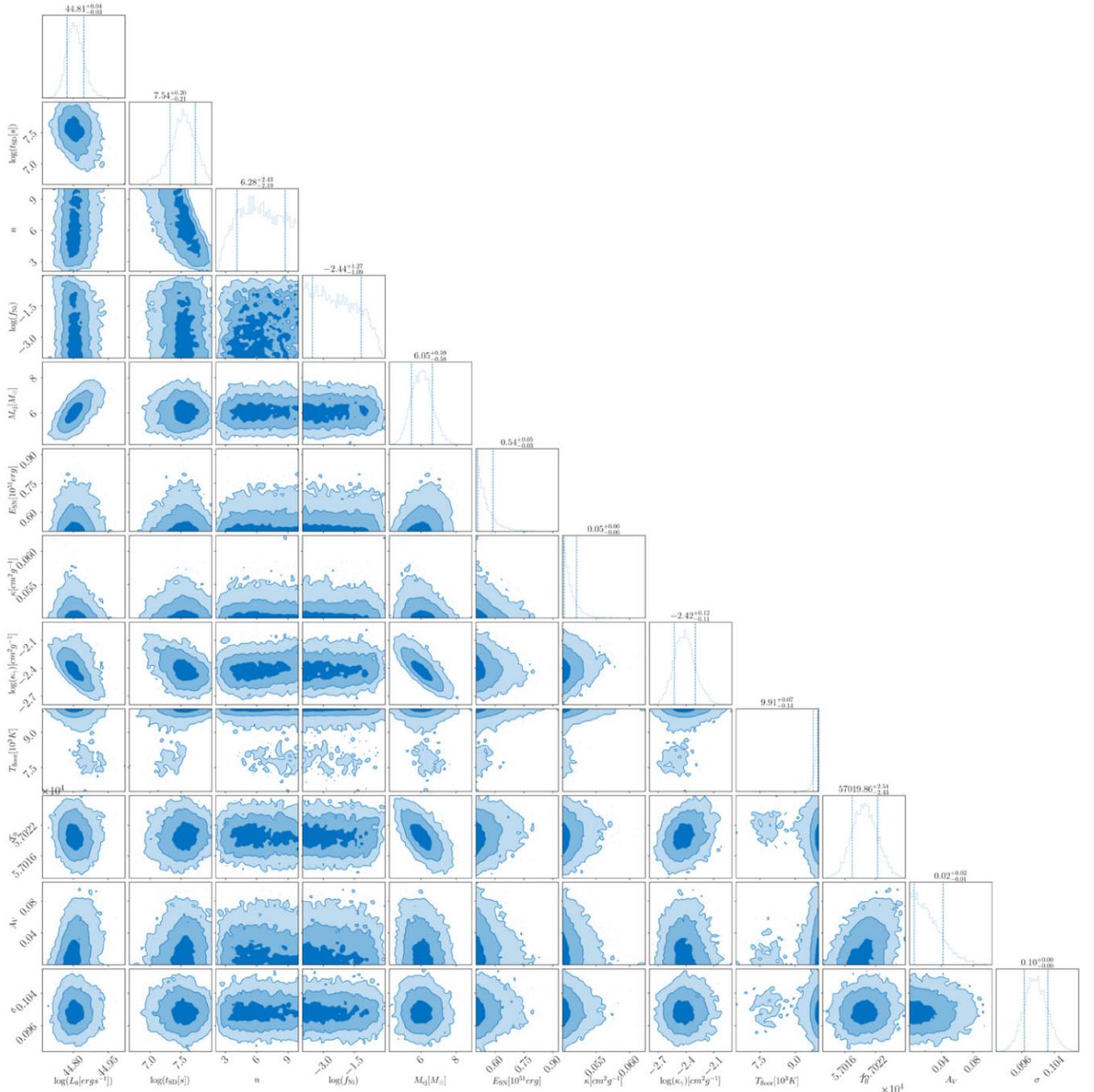**Figure A1.** Corner plot for the simulated SLSN. Injected values are shown in orange.

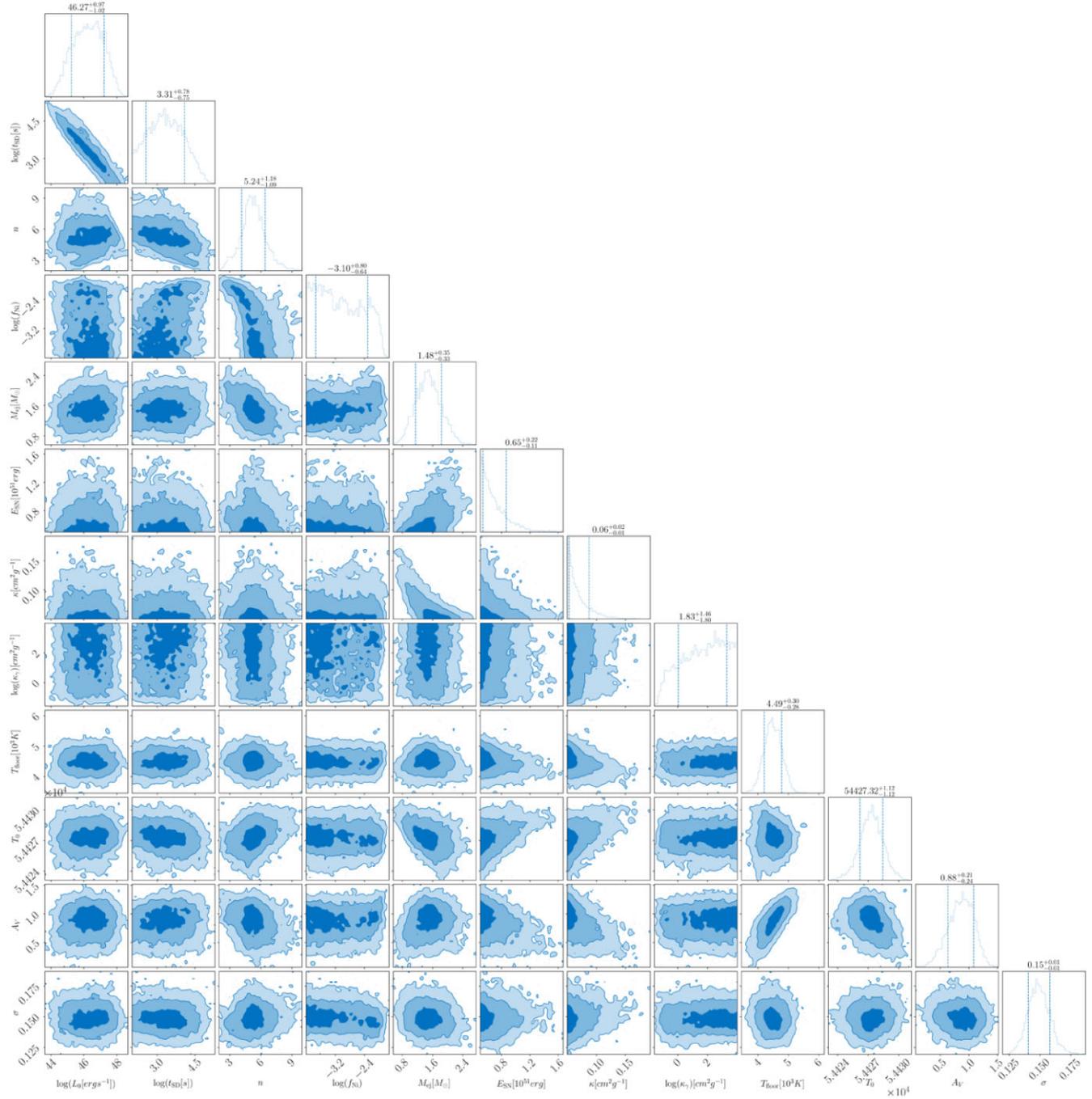**Figure A2.** Corner plot for SN 2015bn, an SLSN.

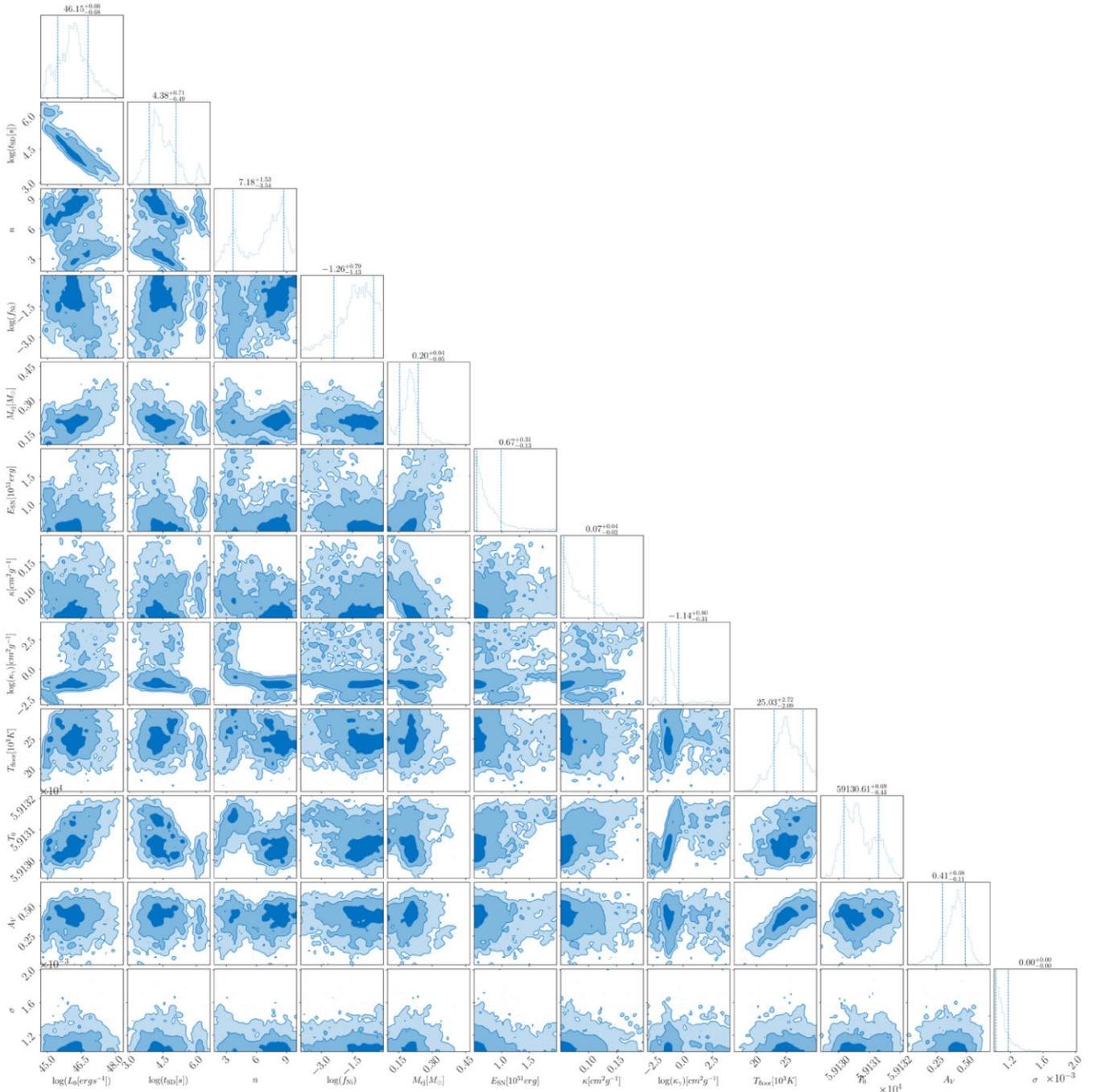**Figure A3.** Corner plot for SN 2007ru, an SN Ic-BL.

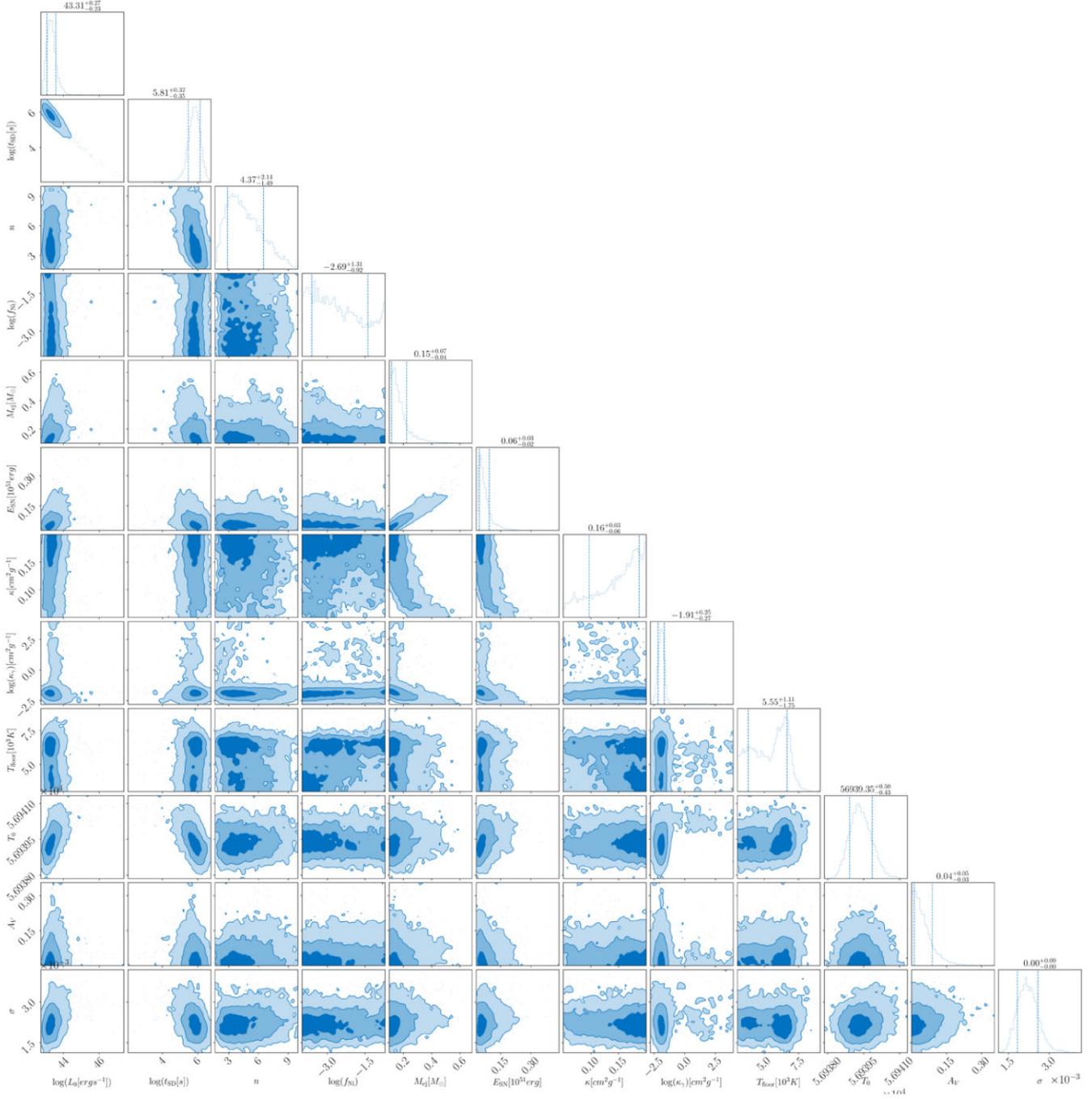**Figure A4.** Corner plot for ZTF20acigmel (the Camel), an FBOT.

Figure A5. Corner plot for iPTF14gqr, a USSN.

This paper has been typeset from a TEX/LATEX file prepared by the author.